Available online at www.sciencedirect.com

SciVerse ScienceDirect

Geochimica et Cosmochimica Acta 90 (2012) 12–32

Geochimica et Cosmochimica Acta

www.elsevier.com/locate/gca

Controls on PGE fractionation in the Emeishan picrites and basalts: Constraints from integrated lithophile–siderophile elements and Sr–Nd isotopes

Chusi Li [a,b,*], Yan Tao [a], Liang Qi [a], Edward M. Ripley [b,*]

[a] State Key Laboratory of Ore Deposit Geochemistry, Institute of Geochemistry, Chinese Academy of Sciences, Guiyang 550002, China
[b] Department of Geological Sciences, Indiana University, Bloomington, IN 47405, USA

Received 22 February 2012; accepted in revised form 22 April 2012; available online 8 May 2012

Abstract

Picrites from the Emeishan large igneous province (ELIP) may be divided into those that show LREE enrichment and those that are characterized by LREE depletion. All picrite types have low $^{87}Sr/^{86}Sr$ ratios (<0.7057) but variable ε_{Nd}, suggesting that crustal contamination has been negligible, and source mantle variation is responsible for their chemical diversity. In contrast, coeval basalts show strong signatures of crustal contamination. Calculated mantle potential temperatures are 240 °C higher than that in ambient mantle, supporting a plume origin for the province. A depleted plume source and ancient sub-continental lithospheric mantle are inferred to be the most important end-members involved in the generation of the Emeishan picrites. Pt and Pd values of the picrites show no evidence of depletion; Pt/Pd ratios are highly variable and show no correlation with picrite type. PGE analyses of both picrites and coeval basalts confirm that Os, Ir, and Ru (IPGE) have behaved compatibly and Pt, Pd, and Rh have behaved incompatibly during Cr-spinel and olivine crystallization. PGE-depleted basalts are present in the ELIP, but the most fractionated basalts tend not to show significant depletion in Pt and Pd. This suggests that fractional crystallization alone was not sufficient to induce sulfide saturation in the magmas, and that contamination involving crustal sulfur was an important driving mechanism. Significant depletion of Ir relative to Ru in some of the basalts regardless of the sulfide saturation state of the parental magma suggests that Ir-dominant alloys segregated prior to magma eruption. Depletions of IPGE relative to Pt and Pd in the Emeishan picrites are consistent with the notion that IPGE alloys are stable in the mantle during partial melting.

1. INTRODUCTION

The Permian Emeishan large igneous province (ELIP) in southwest China has attracted considerable attention because (1) it is contemporaneous with the end-Guadalupian mass extinction (e.g., Zhou et al., 2002), (2) it hosts several magmatic Ni–Cu–PGE (platinum group elements) deposits (e.g., Tao et al., 2007, 2008, 2010) and some of the largest Fe–Ti–V oxide deposits in the world (e.g., Zhou et al., 2008; Pang et al., 2009; Zhong et al., 2011a,b), and (3) it provides excellent samples to study the role of source mantle heterogeneity and plume–lithosphere interaction in magma differentiation and metallogeny. Many researchers have used whole-rock major and trace element compositions and Sr–Nd–Os isotopes of basalts and picrites (whole-rock MgO > 16 wt.% and lack of olivine spinifex texture) to investigate the last aspect (e.g., Chung and Jahn, 1995; Xu et al., 2001; Song et al., 2001, 2008; Xiao et al., 2004; Hanski et al., 2004, 2010; Zhang et al., 2006, 2008; Li et al., 2010; Anh et al., 2011). Some researchers have also used PGE as complementary data (Zhang et al., 2005; Song et al., 2006, 2009; Wang et al., 2007, 2011; Qi and Zhou, 2008; Qi et al., 2008). The PGE studies are mainly focused on basalts; only four picrite samples from the entire ELIP, one from the

* Corresponding authors.
E-mail addresses: cli@indiana.edu (C. Li), ripley@indiana.edu (E.M. Ripley).

0016-7037/$ - see front matter © 2012 Elsevier Ltd. All rights reserved.
http://dx.doi.org/10.1016/j.gca.2012.04.046

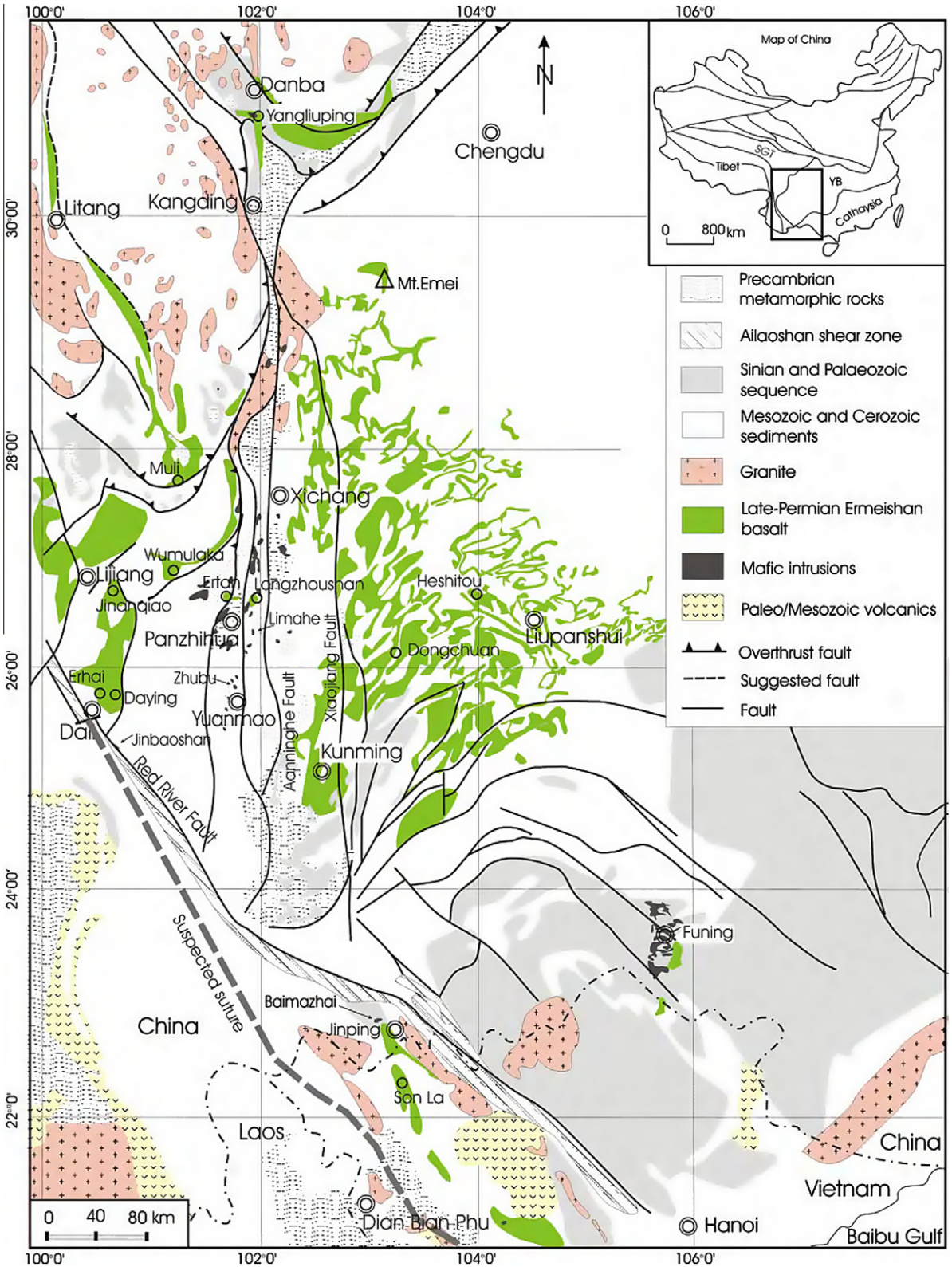

Fig. 1. Distribution of Emeishan flood basalts and coeval mafic intrusions (modified from Chung and Jahn (1995) and Song et al. (2001)). The suspected suture shown as proposed by Chung et al. (1997).

Jinping-Song Da region (Wang et al., 2007) and the rest from the Lijiang region (Zhang et al., 2005), have been analyzed for PGE. There are also some Os concentration data obtained in Re–Os isotope studies (Hanski et al., 2004; Zhang

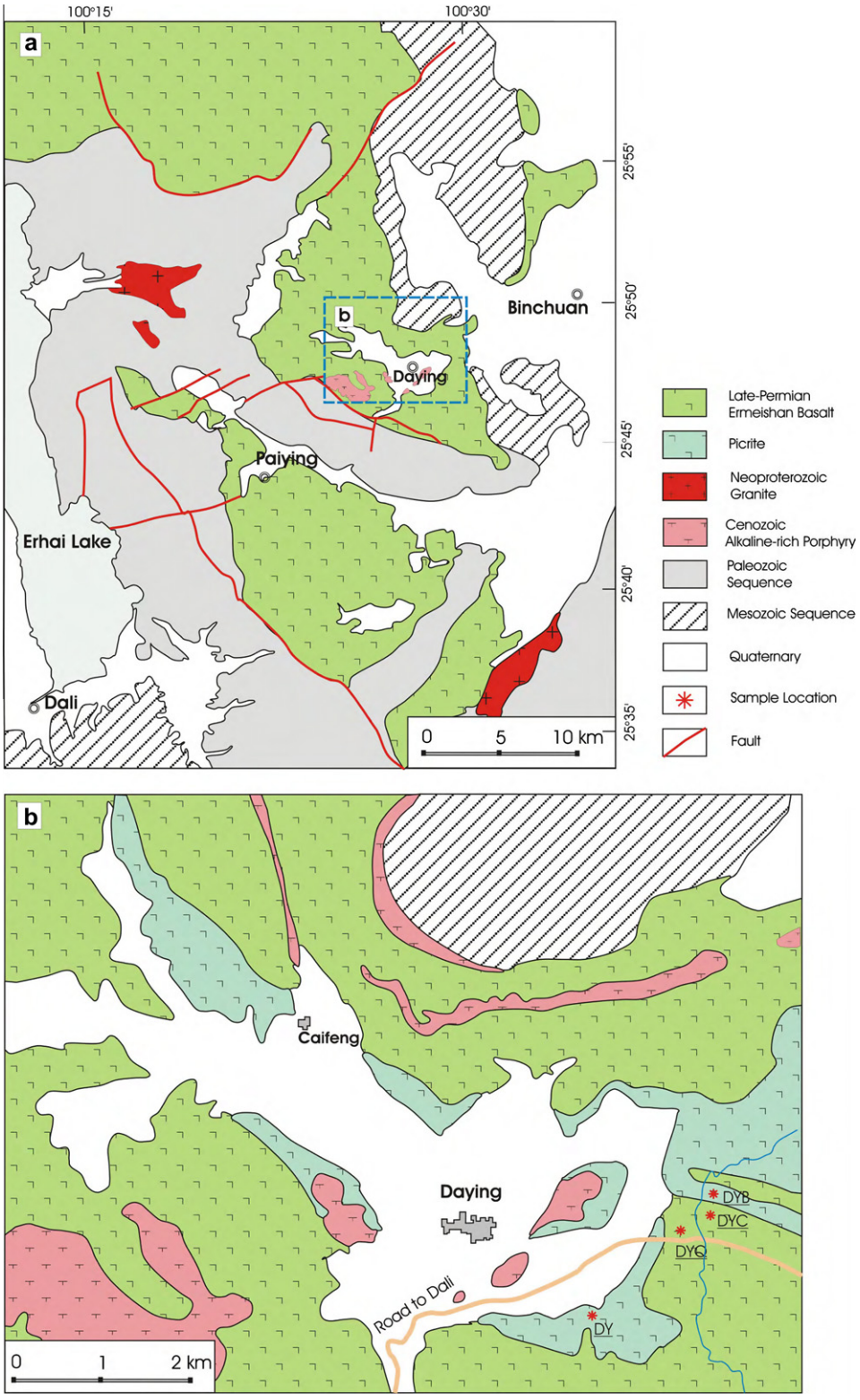

Fig. 2. Distribution of Emeishan flood basalts (a) and associated picrites (b) in the Daying area (modified from TGT-YBGR (1993)). Sample locations are shown in (b).

et al., 2008; Li et al., 2010). To gain a broader view we have analyzed 14 new picrite samples, plus 17 new basalt samples from the Daying, Ertan and Wumulaka areas for PGE plus trace elements and Sr–Nd isotopes. The new data, together with the previous data, are used to address several outstanding questions such as: (1) do different source mantle compo-

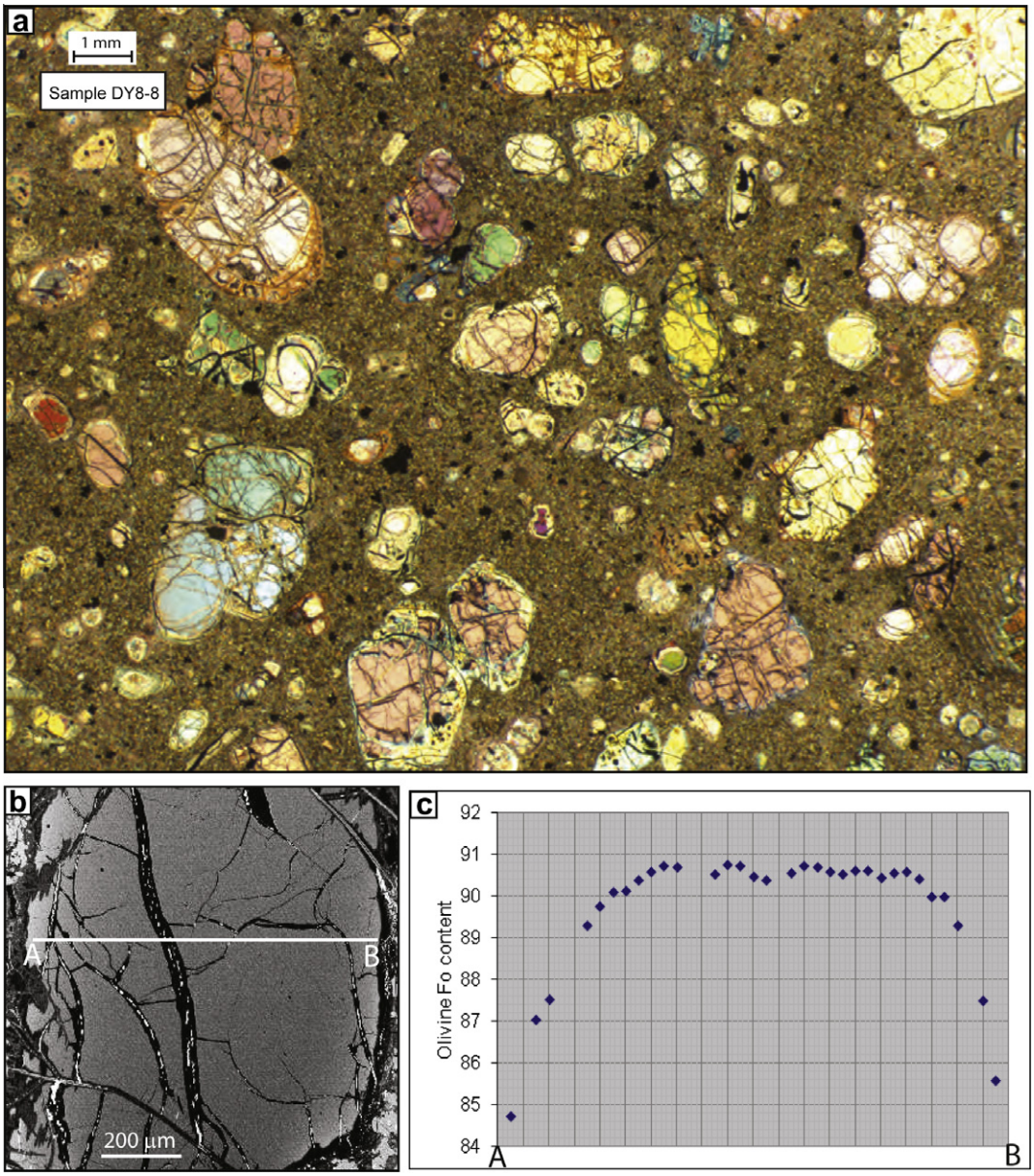

Fig. 3. Photomicrograph of a picrite (a), back-scattered electron image of an olivine phenocryst (b) and variation of Fo contents across the phenocryst (c).

nents have dramatically different Pt/Pd ratios, (2) what are the controls of the fractionation of PGE during mantle melting and fractional crystallization during magma ascent, and (3) which process, fractional crystallization or crustal contamination, is more important in triggering sulfide saturation in magma? In this paper, we begin with using new $^{40}Ar/^{39}Ar$ age data and field observations to confirm that the Daying picrites are indeed part of the Emeishan volcanic succession, and not Cenozoic picritic porphyries as suggested by some researchers (e.g., Zhang et al., 2006). In addition, we use a novel approach based on olivine–liquid relations and mass balance to estimate the composition of primary magma for a primitive picrite. The composition of the primary magma is then used to calculate mantle potential temperature and the degree of partial melting, and to assess whether or not sulfides were present in the mantle residue of high-Mg primary magma.

2. GEOLOGICAL BACKGROUND

Voluminous flood basalts and numerous coeval mafic–ultramafic intrusions of Permian ages (~260 Ma, Zhou et al., 2002) in southwest China are collectively referred to as the Emeishan large igneous province (ELIP) (Fig. 1). The name Emeishan, which means Mt. Emei, has been chosen because Mt. Emei is a popular tourist attraction and a household name in China. In addition, the upper parts of Mt. Emei are flood basalts studied by many pioneer researchers.

The mafic–ultramafic intrusions are exposed in the central region of the ELIP due to severe post-eruptional uplifting and erosion (Fig. 1). Several relatively small and primitive intrusions contain important Ni–Cu–PGE sulfide mineralization whereas some of the larger and more evolved intrusions host giant Fe–Ti–V oxide deposits. The genetic links between different types of intrusions and different types of coeval volcanic rocks in the ELIP still remain elusive (Zhou et al., 2008).

The volcanic rocks of the ELIP are present in a large region of (3–4) $\times 10^5$ km^3 from southwest China to northern Vietnam (e.g., Xu et al., 2001; Xiao et al., 2004; Ali et al., 2010). The area estimation generally accommodates the E–W shortening induced by a number of Mesozoic folding episodes as well as middle to late Cenozoic thrust stacking related to the continuing collision of India into Asia (e.g., Ali et al., 2004), and the southward crustal extrusion, which took place during the last phase of orogeny (i.e., the India-Asia collision), in particular the Red River–Song Da system (e.g., Chung et al., 1997).

The Emeishan volcanic succession comprises predominantly basaltic lavas and has a thicknesses varying from several hundred meters up to 5000 m (Xu et al., 2001; Xiao et al., 2004). To date picrites have only been found in the west (Dali, Lijiang, Muli) and in the south (Jinping-Song Da) (Fig. 1). The picrite samples used in this study are from the Wumulaka area west of Lijiang and from the Daying area northeast of Dali (Fig. 1). As shown in this work, the picrites in the Daying area are parts of the Emeishan volcanic succession (Figs. 2a and b). The basalts used in this study are from the Daying area and several other localities in the western part of the ELIP.

3. ANALYTICAL METHODS

Olivine composition was determined by wavelength-dispersive X-ray emission microanalysis using a CAMECA SX50 electron microprobe in the Department of Geological Sciences at Indiana University. Analytical conditions for major elements were 15 keV accelerating voltage, 20 nA beam current, 1 μm beam size and peak counting time of 20 s. Calcium and Ni in olivine were analyzed using a beam current of 100 nA and a peak counting time of 100 s. Under these conditions the detection limits were estimated to be 20 ppm Ca and 80 ppm Ni. Matrix effects were corrected using the PAP program supplied by CAMECA. Analytical reproducibility was within ±2% relative standard deviation. The accuracy of the analyses was monitored using an international olivine standard (San Carlos olivine, USNM 1113122/444).

Major element compositions of olivine separates and whole-rocks were analyzed by XRF using an AXIOS-PW4400 instrument in the Institute of Geochemistry, Chinese Academy of Sciences, Guiyang. The analytical accuracies are estimated to be ±2% (relative) for major oxides present in concentrations greater than 0.5 wt.% and ±5% (relative) for minor oxides present in concentrations between 0.1 wt.% and 0.5%. Whole-rock trace element compositions were analyzed in the Institute of Geochemistry, Chinese Academy of Sciences, Guiyang, using inductively coupled plasma mass spectrometry (ICP-MS) after a 12-h digestion with a mixture of HF and HNO_3 acids in high-pressure bombs following the procedure of Liang et al. (2000). The accuracies of the ICP-MS analyses were estimated to be better than ±5% (relative) for most elements. Platinum, Pd, Ru, Ir and Os were measured by isotope dilution (ID)-ICP-MS using an improved Carius tube technique (Qi et al., 2007) in the Institute of Geochemistry, Chinese Academy of Sciences, Guiyang. The mono-isotope element Rh was measured by external calibration using a ^{194}Pt spike as the internal standard (Qi et al., 2004). Ten grams of rock powder was digested with ~40 ml aqua regia in a 75 ml Carius tube placed in a sealed, custom-made, high-pressure, water-filled autoclave. After digestion at 300 °C, Os was distilled in a custom-made system, and the residual solution was used to collect PGE by Te-coprecipitation (Qi et al., 2004). The total procedural blanks were lower than 0.001 ppb for Os; 0.003 ppb for Ir, Ru and Rh; 0.02 ppb

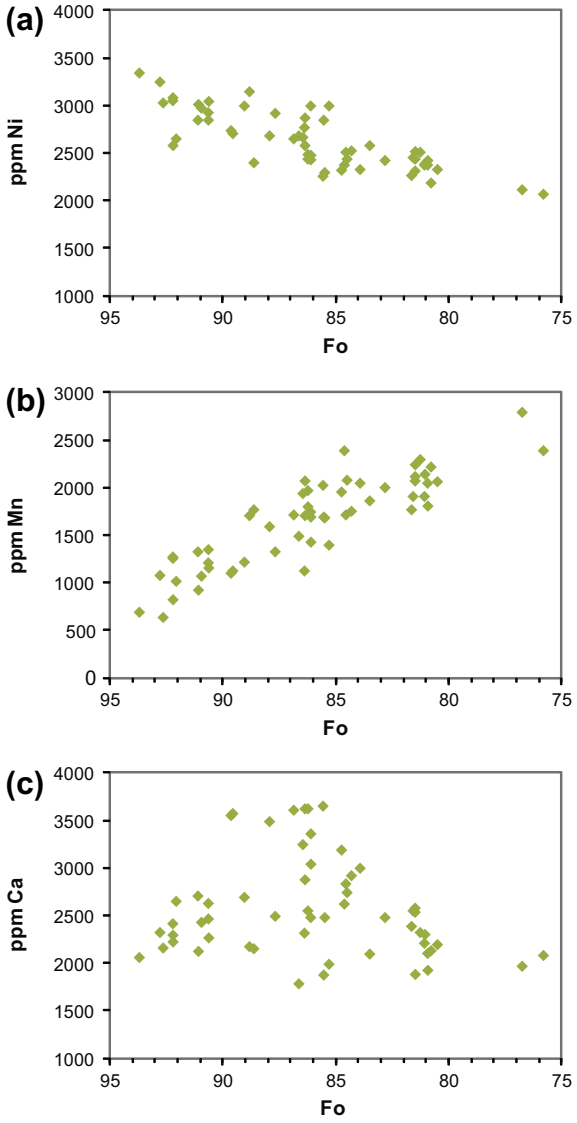

Fig. 4. Relationships between Ni (a), Mn (b), Ca (c), and Fo contents in olivine phenocrysts of picrites from Daying and Wumulaka areas.

Table 1
Major and trace element concentrations in whole rocks.

Sample	DYB-1	PY2	PY5	ErR2-7	LZh-2	YSB6-3	XL6	DYQ1-1	DYQ1-4	DYC-9	DYB-19
Location	Daying			Ertan	Longzhushan	Jinanqiao	Wumulaka	Daying			
Rock type	Alkaline basalt							Subalkaline basalt			
Oxide (wt.%)											
SiO_2	46.58	46.77	43.42	48.48	48.70	48.64	47.52	48.23	48.47	48.69	47.56
TiO_2	3.76	1.67	1.78	2.26	3.54	3.32	3.70	2.17	2.11	1.60	1.90
Al_2O_3	12.27	13.35	13.76	11.66	12.86	15.83	12.85	13.19	13.30	13.77	14.55
Fe_2O_3	16.09	13.08	12.54	12.37	11.94	12.26	14.17	11.30	11.51	11.28	14.23
MnO	0.21	0.15	0.19	0.17	0.16	0.20	0.21	0.18	0.18	0.15	0.30
MgO	5.07	5.55	5.85	8.40	5.93	4.03	4.85	6.77	7.22	7.72	8.28
CaO	7.35	9.81	12.44	8.77	9.59	4.78	7.05	9.70	8.33	10.18	7.32
Na_2O	3.53	3.37	2.47	2.86	2.59	4.41	3.65	2.73	3.05	1.88	2.94
K_2O	1.47	0.84	0.42	1.61	1.61	1.94	1.28	1.00	1.17	0.75	0.33
P_2O_5	0.41	0.34	0.51	0.23	0.37	0.41	0.36	0.28	0.27	0.15	0.12
LOI	2.48	3.66	6.06	2.36	2.28	5.16	2.94	3.17	3.23	2.51	3.89
Total	99.21	98.59	99.43	99.17	99.58	100.97	98.57	98.71	98.83	98.67	101.43
Mg#	0.38	0.45	0.47	0.57	0.49	0.39	0.40	0.53	0.55	0.57	0.53
Trace element (ppm)											
Sc	31.8	33.2	28.3	32.7	27.6	21.6	28.4	33.8	32.9	32.8	42.1
V	472	383	356	312	303	242	393	317	299	243	399
Cr	120	28	55	448	271	58	131	429	426	688	388
Co	61.4	66.5	184.9	52.4	44.0	47.3	41.0	41.0	39.2	80.2	76.4
Ni	96.0	86.6	74.7	156.3	49.5	63.6	85.8	24.1	23.1	37.0	203
Cu	170	157	125	29.1	134	79.1	450	39.7	37.4	39.8	47.0
Zn	201	140	152	99.4	117	152	158	105	106	96.7	111
Ga	31.0	21.4	19.8	19.0	19.4	23.9	25.1	21.9	18.3	18.5	24.9
Rb	45.6	15.9	11.3	33.5	49.2	32.4	27.6	38.7	51.0	16.0	15.0
Sr	650	145	328	329	702	329	412	488	466	231	1367
Y	40.9	28.5	25.9	19.8	23.0	25.4	36.9	30.6	28.4	19.4	27.1
Zr	321	117	117	187	295	310	306	200	192	97.7	175
Nb	34.5	13.9	17.2	34.4	42.5	33.5	35.2	17.2	16.6	7.0	22.1
Ba	262	89.6	103	683	511	898	486	365	322	179	88.5
La	27.7	10.4	10.7	36.3	42.3	41.7	43.6	31.6	27.5	9.3	16.4
Ce	64.1	21.4	23.0	74.3	94.6	90.9	91.8	67.8	62.6	20.7	35.0
Pr	8.51	3.05	3.01	8.92	12.42	11.20	11.27	8.43	8.01	2.73	4.65
Nd	37.5	13.1	12.0	37.8	53.1	47.1	48.5	36.2	33.1	10.4	18.5
Sm	8.13	3.92	3.65	6.53	9.46	9.05	9.98	7.70	7.50	2.97	4.41
Eu	2.69	1.37	1.36	2.14	2.92	2.58	2.96	2.06	1.97	1.08	1.59
Gd	7.10	3.81	3.54	5.88	8.20	7.48	9.46	7.84	7.20	2.83	4.11
Tb	1.10	0.67	0.59	0.79	1.03	1.04	1.35	1.07	1.05	0.47	0.70
Dy	6.84	4.54	4.06	4.00	5.31	5.40	7.19	6.25	6.02	3.05	4.45
Ho	1.34	0.89	0.81	0.73	0.86	0.96	1.32	1.18	1.09	0.65	0.89
Er	3.46	2.37	2.23	2.06	2.24	2.45	3.38	3.29	3.15	1.70	2.31

(*continued on next page*)

Table 1 (*continued*)

Sample	DYB-1	PY2	PY5	ErR2-7	LZh-2	YSB6-3	XL6	DYQ1-1	DYQ1-4	DYC-9	DYB-19
Location	Daying			Ertan	Longzhushan	Jinanqiao	Wumulaka	Daying			
Rock type	Alkaline basalt							Subalkaline basalt			
Tm	0.49	0.32	0.30	0.26	0.28	0.30	0.44	0.43	0.42	0.23	0.33
Yb	2.67	2.00	1.95	1.77	1.80	1.85	2.80	2.76	2.74	1.44	2.01
Lu	0.37	0.31	0.27	0.23	0.22	0.26	0.40	0.40	0.34	0.20	0.31
Hf	5.51	2.19	2.29	4.73	7.24	7.32	7.66	5.20	4.95	1.81	3.22
Ta	1.99	0.73	0.79	2.02	2.71	2.04	2.21	1.14	1.12	0.45	1.23
Pb	3.73	1.32	3.68	10.06	4.12	13.78	6.27	3.99	3.15	0.11	4.72
Th	2.97	1.25	1.46	5.15	5.08	6.53	4.88	7.51	7.13	1.44	2.85
U	0.75	0.33	0.44	1.03	1.36	1.40	1.21	1.54	1.62	0.35	0.47
	YSB3-3	EH2	EH7-1	EH14-1	EM-7	GYH3	DY1-1	DY4-1	DY7-5	DY8-3	DY8-7
	Jinanqiao	Erhai			Emei	Liupanshui	Daying				
	>Subalkaline basalt						Picrite				
Oxide (wt.%)											
SiO_2	47.69	46.91	45.89	48.68	48.83	48.73	41.69	42.86	41.60	41.96	41.17
TiO_2	2.41	1.88	1.70	4.47	3.87	2.01	1.35	1.60	1.54	0.75	0.68
Al_2O_3	13.42	13.09	13.75	12.50	13.49	13.77	6.54	7.58	7.91	8.64	8.01
Fe_2O_3	13.08	12.55	14.07	14.14	14.02	12.96	12.83	12.36	12.18	11.17	11.13
MnO	0.17	0.14	0.28	0.20	0.19	0.21	0.15	0.16	0.14	0.15	0.13
MgO	5.37	5.22	6.04	4.50	4.75	6.03	24.61	19.91	19.26	22.28	23.78
CaO	10.58	11.51	10.36	9.23	8.61	10.95	6.57	9.14	9.16	7.67	7.14
Na_2O	2.35	3.66	3.16	2.08	1.88	2.20	0.87	1.11	1.22	0.97	0.86
K_2O	1.23	0.03	0.06	0.77	1.20	0.43	0.43	0.95	0.62	0.22	0.21
P_2O_5	0.26	0.24	0.23	0.52	0.42	0.21	0.18	0.27	0.26	0.17	0.15
LOI	2.15	3.40	3.46	1.57	2.77	1.71	3.50	2.98	4.35	4.74	5.12
Total	98.71	98.63	99.00	98.65	100.03	99.19	98.71	98.90	98.24	98.70	98.38
Mg#	0.44	0.44	0.45	0.38	0.39	0.47	0.79	0.76	0.75	0.79	0.80
Trace element (ppm)											
Sc	27.8	40.9	42.6	34.0	25.6	39.1	20.7	28.2	31.7	30.8	37.6
V	390	407	462	428	391	340	183	239	209	199	165
Cr	94	340	84	93	95	261	2185	1434	1404	2038	2311
Co	53.5	56.4	60.6	46.3	41.3	44.8	109	82.2	87.5	87.1	96.4
Ni	95.6	170	83.0	71.5	68.3	109	1434	857	857	1002	1203
Cu	254	45.4	33.5	297	219	184	23.1	128	106	97.9	72.2
Zn	112	122	136	209	163	121	88.1	109	92.8	80.8	68.1
Ga	21.9	21.3	22.7	30.2	25.7	20.2	9.9	11.6	12.7	10.0	11.1
Rb	34.0	0.4	1.1	21.0	27.5	10.6	18.1	30.9	19.5	14.3	18.3
Sr	681	169	193	443	581	276	213	657	391	188	175
Y	22.8	25.2	27.0	50.6	35.0	27.9	13.3	14.5	14.0	13.4	11.5
Zr	187	110	99	447	376	146	126	118	114	55.2	46.9
Nb	31.0	10.5	10.6	50.5	37.6	14.1	19.3	32.5	29.9	11.2	8.8

Ba	425	15.6	41.9	416	554	220	140	2182	449	134	165
La	34.1	7.6	7.5	46.5	48.0	19.4	17.8	32.2	33.6	15.6	14.5
Ce	69.6	17.8	17.3	99.8	109.0	41.4	38.8	59.9	61.3	31.1	27.5
Pr	8.1	2.5	2.4	12.8	13.5	5.4	4.7	6.9	6.4	3.7	3.1
Nd	34.7	10.9	9.6	55.5	56.6	22.8	19.6	27.0	24.2	14.8	12.0
Sm	6.18	3.49	3.22	10.91	11.83	5.41	3.92	4.38	3.92	3.08	2.27
Eu	2.03	1.28	1.26	3.26	3.32	1.71	1.22	1.47	1.16	0.99	0.72
Gd	6.00	3.68	3.34	9.77	10.76	5.87	3.71	4.71	4.37	3.16	2.75
Tb	0.87	0.63	0.62	1.40	1.47	0.93	0.50	0.56	0.70	0.45	0.47
Dy	4.45	4.43	3.97	8.41	8.00	5.64	2.73	3.15	2.79	2.64	2.22
Ho	0.86	0.86	0.88	1.62	1.42	1.09	0.51	0.61	0.55	0.55	0.45
Er	2.31	2.27	2.23	4.07	3.82	3.30	1.35	1.55	1.68	1.49	1.32
Tm	0.28	0.33	0.34	0.54	0.50	0.45	0.17	0.23	0.20	0.21	0.15
Yb	1.91	1.80	2.00	3.23	3.06	2.90	1.12	1.30	1.15	1.28	1.01
Lu	0.25	0.25	0.30	0.50	0.43	0.44	0.16	0.18	0.18	0.19	0.15
Hf	4.67	2.31	1.99	7.91	9.43	3.92	3.15	3.05	3.26	1.43	1.69
Ta	1.82	0.59	0.52	2.85	2.54	0.93	1.32	1.86	1.74	0.59	0.48
Pb	5.33	3.04	2.25	5.41	13.22	4.40	102.4	5.66	3.89	3.58	2.15
Th	5.13	0.80	0.81	6.20	7.75	3.04	2.38	4.13	4.22	2.19	1.67
U	1.25	0.27	0.15	1.53	1.71	0.75	0.56	0.83	0.71	0.44	0.33

	DY8-8	DY10-1	LSTZ-1	LSTZ-2	DYB2-2	DYB-13	ErR2-15	XL5	XL11-3	XL12	XL14
	Daying Picrite						Ertan	Wumulaka			
Oxide (wt.%)											
SiO_2	41.65	44.21	41.89	42.37	41.24	41.87	45.28	44.40	42.83	44.23	45.42
TiO_2	0.74	2.31	0.79	0.73	0.55	0.52	1.91	2.47	1.80	2.44	2.36
Al_2O_3	8.37	7.89	8.83	9.17	7.33	6.86	8.16	8.10	9.20	7.23	7.43
Fe_2O_3	11.20	13.00	11.16	11.57	11.12	10.98	12.40	13.56	13.15	13.47	13.13
MnO	0.14	0.16	0.14	0.15	0.13	0.14	0.15	0.17	0.17	0.17	0.17
MgO	22.48	18.07	21.41	20.89	25.59	26.61	17.75	18.07	18.14	17.72	18.07
CaO	7.60	8.01	7.38	9.44	6.51	6.75	7.28	8.12	7.51	8.10	8.71
Na_2O	0.84	1.46	0.79	1.14	1.11	0.70	0.71	1.47	1.48	1.81	1.48
K_2O	0.19	0.72	0.19	0.25	0.24	0.19	2.00	0.79	0.69	0.66	0.84
P_2O_5	0.17	0.25	0.18	0.26	0.13	0.13	0.19	0.22	0.25	0.22	0.21
LOI	5.39	2.48	6.01	2.68	4.50	5.23	3.04	2.21	3.84	2.48	1.69
Total	98.76	98.55	98.77	98.65	98.45	99.98	98.87	99.57	99.07	98.53	99.50
Mg#	0.79	0.73	0.79	0.78	0.81	0.82	0.73	0.72	0.73	0.72	0.72
Trace element (ppm)											
Sc	26.5	28.1	33.2	29.5			27.5	29.3	24.0	27.2	28.1
V	184	279	210	191			244	288	273	251	290
Cr	2422	1399	2346	1469			1654	1337	1349	1319	1458
Co	91.1	79.2	119	109			81.1	79.2	81.1	78.4	85.8
Ni	1186	812	1126	759			742	792	849	785	867

(*continued on next page*)

Table 1 (*continued*)

	DY8-8	DY10-1	LSTZ-1	LSTZ-2	DYB2-2	DYB-13	ErR2-15	XL5	XL11-3	XL12	XL14
	Daying Picrite						Ertan	Wumulaka			
Cu	24.6	121	73.5	96.0			99.0	144	122	147	129
Zn	104	111	88.3	67.1			109	118	111	121	130
Ga	8.9	14.9	10.4	10.3			14.3	15.6	16.2	15.9	15.72
Rb	17.6	26.3	23.9	15.4			59.7	17.4	20.0	16.2	16.27
Sr	159	375	195	328			80	404	269	331	475.36
Y	12.9	18.3	15.3	19.1			16.3	17.6	17.4	19.1	19.62
Zr	51.4	193.0	63.3	70.0			168	165	117	171	184.94
Nb	10.9	25.3	12.1	22.4			22.1	26.0	21.2	27.3	26.81
Ba	165	304	178	357			491	256	269	218	257.57
La	13.3	27.6	13.9	32.7			25.5	26.7	16.3	27.7	24.25
Ce	27.0	60.6	27.2	60.6			56.0	56.6	34.8	59.7	51.44
Pr	3.23	7.70	3.20	6.78			6.98	7.04	4.43	7.39	6.44
Nd	13.0	32.0	10.7	24.0			31.2	29.6	20.7	31.9	26.22
Sm	2.71	6.20	2.63	4.37			5.73	5.71	4.34	6.04	5.64
Eu	0.89	1.97	0.88	1.42			1.68	1.82	1.41	1.91	1.82
Gd	2.96	6.37	2.50	4.30			5.42	5.06	4.18	5.66	4.83
Tb	0.43	0.76	0.36	0.61			0.72	0.77	0.67	0.80	0.71
Dy	2.51	4.45	2.36	3.67			3.44	3.83	3.67	3.99	3.91
Ho	0.50	0.78	0.51	0.72			0.66	0.67	0.62	0.75	0.75
Er	1.35	1.93	1.32	1.94			1.72	1.66	1.72	1.85	1.84
Tm	0.19	0.24	0.20	0.27			0.22	0.23	0.23	0.23	0.23
Yb	1.21	1.53	1.08	1.58			1.32	1.31	1.39	1.44	1.30
Lu	0.17	0.21	0.17	0.24			0.18	0.22	0.21	0.17	0.18
Hf	1.44	5.06	1.22	1.58			4.30	4.37	3.05	4.30	3.89
Ta	0.63	1.65	0.54	1.11			1.30	1.65	1.19	1.76	1.67
Pb	98.1	3.97	4.26	4.49			2.93	3.63	4.34	4.76	4.60
Th	2.03	3.52	1.74	4.29			3.12	3.02	1.91	3.24	2.98
U	0.44	0.79	0.35	0.98			0.73	0.65	0.43	0.74	0.68

for Pd; and 0.011 ppb for Pt. The detection limits were estimated to be 0.0002 ppb for Os, 0.001 ppb for Ir, Ru and Rh, 0.009 for Pt and 0.015 for Pd. International standards WPR-1 (peridotite), WGB-1 (gabbro) and TDB-1 (diabase) were used to monitor the accuracy.

The $^{40}Ar/^{39}Ar$ dating of groundmass separated from a picrite (DY4-1) was conducted in the Guangzhou Institute of Geochemistry, Chinese Academy of Sciences, Guangzhou. The sample and a sanidine standard (DRA1) with a recommended age of 25.26 ± 0.07 Ma (Wijbrans et al., 1995) were irradiated at a neutron flow rate of (6–6.5) $\times 10^{12}/cm^2$ per second for 54 h in the 49-2 Reactor, China Institute of Atomic Energy, Beijing. The radiated sample and standard were stepwise heated using a CO_2 laser COHERENT-50W, and the released gas was measured for argon isotopes using a GV Instruments 5400® mass spectrometer. The analytical procedures and data reduction are the same as those described in detail by Qiu and Wijbrans (2008).

Rb–Sr and Sm–Nd isotopic analyses of whole-rock samples were determined using a VG-354 thermal ionization magnetic sector mass spectrometer in the Institute of Geology and Geophysics, Chinese Academy of Sciences, Beijing, using the procedures of Zhang et al. (2001) and Chu et al. (2009), respectively. Mass fractionation corrections for Sr and Nd isotopic ratios were based on values of $^{86}Sr/^{88}Sr = 0.1194$ and $^{146}Nd/^{144}Nd = 0.7219$. Uncertainties in Rb/Sr and Sm/Nd ratio are less than ±0.2% and ±0.5% (relative), respectively.

4. ANALYTICAL RESULTS

4.1. The $^{40}Ar/^{39}Ar$ ages of Daying picrite

The results of $^{40}Ar/^{39}Ar$ dating of groundmass separated from a picrite sample (DY4-1) from the Daying area in the western part of the ELIP (see Fig. 1) are given in Table S1 and Fig. S1. The texture of this sample is similar to another picrite sample from the same area (DY8-8) shown in Fig. 3a. Randomly-orientated olivine phenocrysts of variable sizes are partially altered to serpentine in the margins and micro-fractures. Micro-crystals of pyroxenes and plagioclase in the groundmass are partially altered to chlorite, talc and clay minerals.

The $^{40}Ar/^{39}Ar$ ages of the groundmass separated from the selected picrite sample (DY4-1) vary between 155 and 204 Ma, which are within the range of $^{40}Ar/^{39}Ar$ ages for the Permian Emeishan flood basalts in the region (Ali et al., 2004). The $^{40}Ar/^{39}Ar$ ages of the Daying picrite and most of the Emeishan flood basalts are significantly younger than the zircon U–Pb ages of 255–260 Ma for the mafic–ultramafic intrusions that are thought to be coeval with the volcanic rocks (e.g., Lo et al., 2002; Zhou et al., 2002; Zhong et al., 2011a,b). This is due to pervasive hydrothermal alteration associated with several tectonic events which took place in SW China from the Mesozoic to Cenozoic (Ali et al., 2004).

The majority of researchers in China believe that the Daying picrites are parts of the Permian Emeishan volcanic succession (e.g., Chung and Jahn, 1995; Xu et al., 2001; Song et al., 2001; Hanski et al., 2010). However, this interpretation seems inconsistent with the information shown in an old geological map produced by the Third Geological Team, Yunnan Bureau of Geology and Resources (TGTYBGR, 1993), in which some of the picrites in the Daying area are labeled as Cenozoic picritic porphyry. This has led Zhang et al. (2006) to question all other researchers' view that the Daying picrites are coeval with the Permian Emeishan flood basalts. Given that the Daying picrites can only be either Permian or Cenozoic based on the known history of mafic–ultramafic magmatism in the region (TGTYBGR, 1993), the much older $^{40}Ar/^{39}Ar$ ages of the selected picrite sample (DY4-1) from the Daying areas than the Cenozoic (<65 Ma), plus the fact that the Daying picrites that we have examined are all located within the Permian flood basalt sequence (Fig. 2), indicate that the Daying picrites are indeed part of the Permian Emeishan volcanic succession.

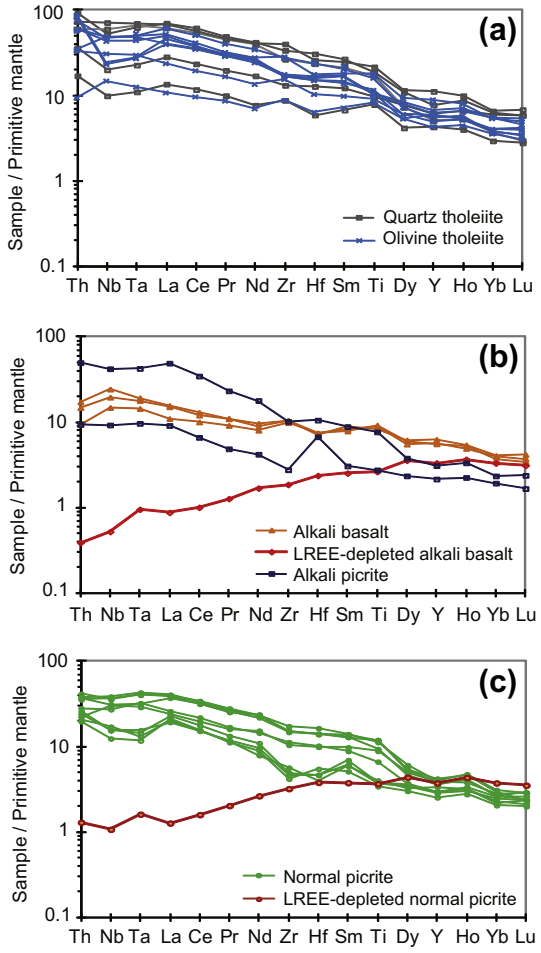

Fig. 5. Primitive mantle-normalized alteration-resistant trace element patterns of basalts and picrites from the Emeishan large igneous province. Data for the LREE-depleted samples are from Wang et al. (2007); the rest are from this study. The primitive mantle values for normalization are from Sun and McDonough (1989).

4.2. Olivine chemistry

The chemical compositions of olivine phenocrysts in the picrite samples from the Daying and Wumulaka areas are given in Table S2. In thin sections olivine phenocrysts vary from <20 μm to >2 mm (Fig. 3a). Small Cr-spinel inclusions are present in some of relatively large olivine phenocrysts. The compositions of the Cr-spinel inclusions are given in Li et al. (2008). The proportions of olivine phenocrysts and groundmass in a representative picrite sample (DY8-8, Fig. 3a) estimated using area measurement software are 41% and 59%, respectively. All large olivine phenocrysts are zoned (Fig. 3b), with core-rim Fo contents varying up to 7 mol% (Fig. 3c). The most significant change of the Fo contents in a large phenocryst occurs at a rim of ~20 μm in thickness. The much larger core, commonly 5–8 times thicker than the rim in thin sections (Fig. 3b), is characterized by rather constant Fo contents (Fig. 3c). The maximum measured Fo content of large olivine phenocrysts is 93 mol%. Significant compositional zoning is not observed in small grains with diameters <30 μm across. The Fo contents of such small grains are similar to the rim compositions of larger grains in a given sample.

Olivine phenocrysts in the picrites from the Daying and Wumulaka areas are characterized by a positive Ni–Fo correlation (Fig. 4a), negative Mn–Fo correlation (Fig. 4b), and variable Ca contents from 1700 to 3600 ppm with no correlation with Fo contents (Fig. 4c). The concentrations of Ca in the Daying and Wumulaka olivine phenocysts are significantly higher than that of mantle olivine (<1000 ppm Ca, Simkin and Smith, 1970; Li et al., 2012 and references therein). The zoning patterns and compositional variations of olivine phenocrysts in the picrites from the Daying and Wumulaka areas are remarkably similar to those from elsewhere in the ELIP reported previously by Hanski et al. (2010).

4.3. Major and trace element abundances in whole-rocks

Whole-rock major and trace element compositions of basalts and picrites from this study are listed in Table 1. The contents of MgO in the samples vary from 4 to 27 wt.%. Many researchers have classified the Emeishan flood basalts into a high-Ti and a low-Ti series based on whole-rock TiO_2 contents and Ti/Y ratios (e.g., Xu et al., 2001; Xiao et al., 2004). This classification is not helpful in probing mantle heterogeneity or the degrees of partial melting (Hou et al., 2011). In the Emeishan flood basalts small Fe–Ti oxide inclusions are common in clinopyroxene phenocrysts. Fractionation of Fe–Ti oxides can change the liquid line of descent and phenocrysts can change the rock composition. To avoid such complication we have adapted

Table 2
Concentrations of Ni, Cu and platinum group elements in whole rocks.

Sample	Location	Rock type	Ni (ppm)	Os (ppb)	Ir (ppb)	Ru (ppb)	Rh (ppb)	Pt (ppb)	Pd (ppb)	Cu (ppm)
DYB-1	Daying	Alkaline basalt	96	0.25	0.13	0.39	0.46	8.04	10.30	170
PY2	Daying	Alkaline basalt	87	0.09	0.03	0.20	0.35	3.26	9.16	157
PY5	Daying	Alkaline basalt	75	0.19	0.02	0.28	0.37	4.63	10.10	125
XL6	Wumulaka	Alkaline basalt	86	0.44	0.29	1.41	0.25	4.19	7.74	450
ErR2-7	Ertan	Alkaline basalt	156	0.37	0.65	0.14	0.34	13.40	6.53	29
LZh-2	Longzhoushan	Alkaline basalt	50	0.03	0.02	0.15	0.02	0.50	0.72	134
YSB6-3	Jinanqiao	Alkaline basalt	64	0.27	0.32	0.09	0.19	3.59	4.63	79
DYQ1-1	Daying	Subalkaline basalt	24	0.08	0.15	0.32	0.02	0.31	0.33	40
DYQ1-4	Daying	Subalkaline basalt	23	0.02	0.04	0.26	0.02	0.24	0.26	37
DYC-9	Daying	Subalkaline basalt	37	0.14	0.03	0.14	0.02	0.08	0.09	40
DYB-19	Daying	Subalkaline basalt	203	0.57	0.52	0.61	0.48	7.94	9.25	47
YSB3-3	Jinanqiao	Subalkaline basalt	96	0.30	0.55	0.42	0.81	13.40	12.00	254
EH14-1	Erhai	Subalkaline basalt	71	0.15	0.10	0.30	0.32	6.75	5.94	297
EH2	Erhai	Subalkaline basalt	170	0.47	0.29	0.66	0.44	7.30	7.79	45
EH7-1	Erhai	Subalkaline basalt	83	0.06	0.04	0.56	0.42	3.03	9.86	34
EM-7	Emei	Subalkaline basalt	68	0.90	0.27	0.20	0.25	6.77	7.74	219
GYH3	Liupanshui	Subalkaline basalt	109	0.15	0.05	0.33	0.39	5.42	10.90	184
DYB2-2	Daying	Picrite	1205	5.07	1.48	3.23	0.67	8.52	5.67	62
DY1-1	Daying	Picrite	1434		1.52	2.31	0.71	5.52	9.55	23
DYB-13	Daying	Picrite	1262	3.78	1.59	2.57	0.69	7.09	3.10	63
DY8-7	Daying	Picrite	1203	2.16	1.09	3.09	0.66	6.58	4.91	72
LSTZ-2	Daying	Picrite	759	2.97	0.87	1.83	0.50	6.13	3.40	96
DY8-3	Daying	Picrite	1002	2.15	1.01	1.83	0.54	6.62	4.05	98
DY8-8	Daying	Picrite	1186		1.26	1.87	0.62	5.29	7.25	25
LSTZ-1	Daying	Picrite	1126	3.35	0.76	1.65	0.42	5.26	3.76	74
DY7-5	Daying	Picrite	857	1.78	0.98	2.30	0.47	7.30	2.72	106
DY10-1	Daying	Picrite	812	3.13	1.30	4.79	0.48	9.29	4.85	121
XL5	Wumulaka	Picrite	792	1.68	0.91	1.76	0.42	9.02	3.96	144
XL11-3	Wumulaka	Picrite	849	1.81	1.09	2.66	0.38	5.52	3.86	122
XL12	Wumulaka	Picrite	785	1.93	1.11	3.31	0.44	9.22	3.50	147
ErR2-15	Ertan	Picrite	742	3.00	1.12	2.23	0.40	10.80	6.55	99

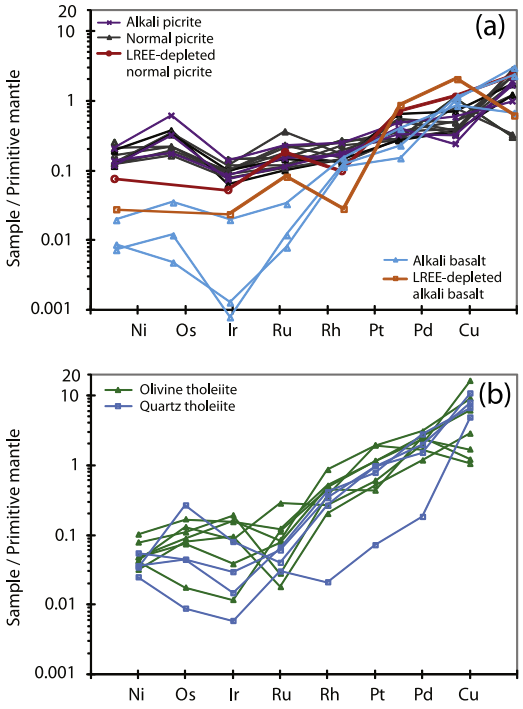

Fig. 6. Primitive mantle-normalized Ni–PGE–Cu patterns of basalts and picrites from the Emeishan large igneous province. Data for the LREE-depleted samples are from Wang et al. (2007); the rest are from this study. The primitive mantle values for normalization are from Barnes and Maier (1999).

the basalt tetrahedron classification of Yoder and Tilley (1962) in which samples with normative nepheline, olivine and quartz are called alkali basalt, olivine tholeiite and quartz tholeiite, respectively. Similarly, picrites with and without normative nepheline are referred to as alkali picrite and normal picrite, respectively. In our normative calculation a whole-rock FeO/Fe_2O_3 ratio of 0.9 was used.

Fig. 5a–c illustrate the primitive mantle-normalized alteration-resistant trace element patterns of the ELIP basalts and picrites from this study plus two LREE-depleted samples from Wang et al. (2007). The Emeishan tholeiites are all enriched in light rare earth elements (LREE) relative to heavy rare earth elements (HREE) (Fig. 5a). The Emeishan alkali basalts can be further divided into two subtypes, LREE-enriched and LREE-depleted (Fig. 5b). Available data indicate that the LREE-depleted alkali basalts only occur in the southernmost region, i.e., the Jinping (SW China)–Song Da (northern Vietnam) region (see Fig. 1) where LREE-depleted picrites are also present. There are more trace element data for the LREE-depleted basalts and picrites (Hanski et al., 2004, 2010; Wang et al., 2007) but for clarity only the samples with PGE data from Wang et al. (2007) are included in the comparison (Fig. 5b and c). Our data show that the Emeishan alkali picrites do not have negative Nb–Ta and Zr–Hf anomalies (Fig. 5b). In contrast, some normal picrites from the ELIP exhibit negative Nb–Ta and Zr–Hf anomalies (Fig. 5c). We can rule out that the presence of negative Nb–Ta and Zr–Hf anomalies in some of our samples is due to incomplete

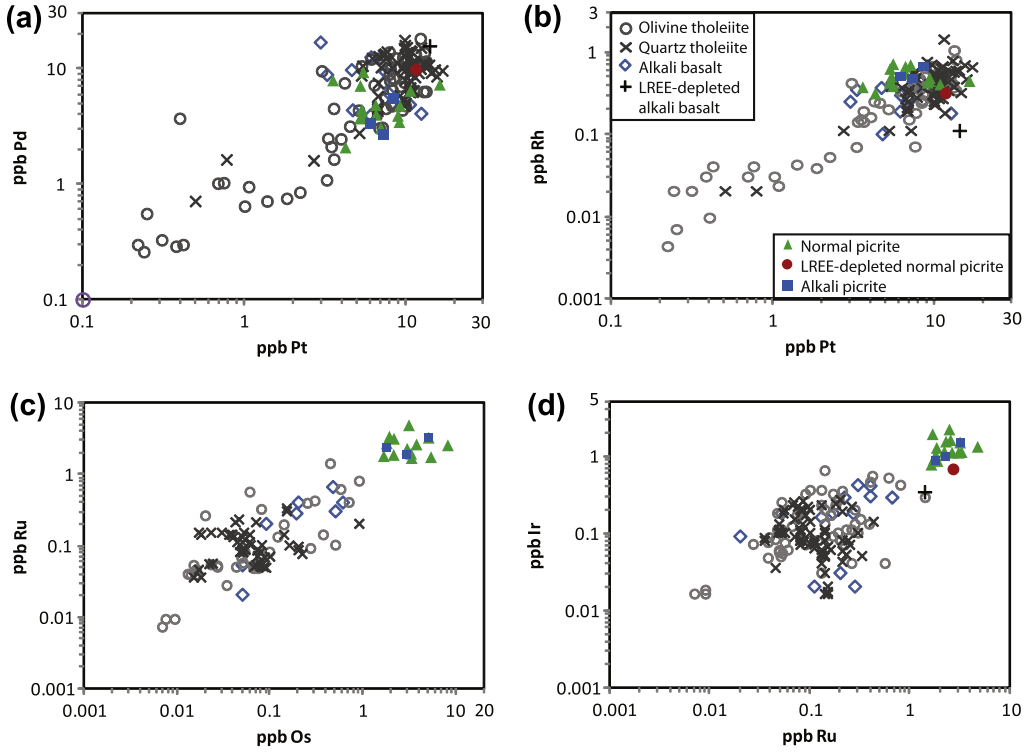

Fig. 7. Correlations between Pt, Pd and Rh (a, b) and between Os, Ir and Ru (c, d). Data are from this study and previous studies given in Table S3.

dissolution of zircon because all our samples were analyzed together using the same procedure.

4.4. Ni, Cu and PGE abundances in whole-rocks

The concentrations of Ni, Cu and PGE in the Emeishan basalts and picrites from this study are listed in Table 2. Fig. 6a–c illustrate the primitive mantle-normalized patterns of Ni, Cu and PGE for the Emeishan basalts and picrites from this study plus the only two LREE-depleted samples that have been analyzed for PGE to date by Wang et al. (2007). The LREE-depleted picrite sample is characterized by moderately fractionated PGE patterns with enrichments of Rh, Pt and Pd relative to Os, Ir and Ru (Fig. 6a). In contrast, all other picrite samples have less fractionated PGE patterns (Fig. 6a). All of the picrite samples show a negative Ir anomaly relative to Os and Ru (Fig. 6a). Three normal picrites including a LREE-depleted sample show a positive Ru anomaly relative to Ir and Rh (Fig. 6a). The LREE-depleted alkali basalt sample also exhibits a positive Ru anomaly (Fig. 6a). Other alkali basalts from the ELIP are characterized by highly fractionated PGE patterns plus a pronounced negative Ir anomaly (Fig. 6a). The coeval tholeiites also have highly fractionated PGE patterns but the negative Ir anomaly is less pronounced and only present in some of the samples (Fig. 6b).

The data from this study together with those from the literature (Table S3) show good positive correlation between Pt, Pd and Rh (Fig. 7a and b), and between Os, Ru and Ir (Fig. 7c and d). No correlations are found between PPGE (Pt, Pd, Rh) and IPGE (Ir, Ru, Os) in the samples. Depletion of Ir relative to Ru is present in some of the samples that contain 0.1–1 ppb Ru (Fig. 7d).

4.5. Sr–Nd isotopes of picrites

The Rb–Sr and Sm–Nd isotopic compositions of the Emeishan picrites from this study are listed in Table 3. The picrite samples analyzed by us are from the Daying and Wumulaka areas in the western parts of the Emeishan flood basalt province (Fig. 1). They all belong to the LREE-enriched type. The ε_{Nd} and initial $^{87}Sr/^{86}Sr$ values ($t = 260$ Ma) vary from 0.06 to 2.53 and from 0.704071 to 0.705152, respectively.

5. INTERPRETATION OF INTEGRATED DATA

To better understand the fundamental controls on PGE fractionation in the Emeishan flood basalts and picrites it is imperative to integrate all available whole-rock major-trace element, PGE and Sr–Nd–Os isotope data. Table S3 is a database we have compiled from the literature (Xiao et al., 2004; Zhang et al., 2005, 2006; Song et al., 2006, 2008, 2009; Wang et al., 2007; Qi and Zhou, 2008; Qi et al., 2008). Sample names and locations listed in the database and shown in Fig. 1 are identical. The distributions of the samples listed in the database geographically cover the entire Emeishan flood basalt province from south (Jinping) to north (Yanliuping), and from east (Liupansui) to west (Lijiang) (see Fig. 1).

Table 3
Rb–Sr and Sm–Nd isotopic compositions of picrites from the Emeishan large igneous province.

Sample	Location	Sm (ppm)	Nd (ppm)	$^{147}Sm/^{144}Nd$	$^{143}Nd/^{144}Nd$	2σ	ε_{Nd}	Rb (ppm)	Sr (ppm)	$^{87}Rb/^{86}Sr$	$^{87}Sr/^{86}Sr$	2σ	$^{87}Sr/^{86}Sr(i)$
DY1-1	Daying	4.51	23.04	0.115957	0.512619	0.000011	2.32	18.01	217.0	0.240253	0.705375	0.000014	0.704487
Dy4-1	Daying	7.84	44.05	0.105436	0.512513	0.000014	0.60	29.16	1038	0.080864	0.705150	0.000013	0.704851
DY8-3	Daying	2.89	13.87	0.123618	0.512517	0.000012	0.07	13.97	179.2	0.224319	0.705265	0.000010	0.704435
DY8-8	Daying	2.98	14.52	0.121663	0.512513	0.000009	0.06	18.11	157.4	0.331130	0.705296	0.000012	0.704071
DY10-1	Daying	8.45	40.01	0.125260	0.512614	0.000012	1.91	21.61	437.9	0.142051	0.705182	0.000010	0.704656
XL5	Wumulaka	8.37	39.54	0.125433	0.512640	0.000012	2.40	16.71	480.4	0.100102	0.704864	0.000011	0.704494
XL11-3	Wumulaka	6.51	27.51	0.140323	0.512615	0.000012	1.43	19.74	390.1	0.145634	0.705691	0.000010	0.705152
XL14	Wumulaka	7.59	35.96	0.125162	0.512646	0.000010	2.53	16.39	564.0	0.083638	0.704837	0.000011	0.704527

Note: λ (^{87}Rb) $= 1.42 \times 10^{-11}$ y^{-1}, λ (^{147}Sm) $= 6.54 \times 10^{-12}$ y^{-1}; $(^{87}Sr/^{86}Sr)_i$, $(^{143}Nd/^{144}Nd)_i$ and ε_{Nd} were calculated relative to present-day chondrite values of $^{143}Nd/^{144}Nd = 0.512638$, $^{147}Sm/^{144}Nd = 0.1967$, $^{87}Sr/^{86}Sr = 0.7045$ and $^{87}Rb/^{86}Sr = 0.0816$, $t = 260$ Ma.

5.1. Mantle heterogeneity and crustal contamination

Compared to the coeval basalts, the picrites of the ELIP have lower initial $^{87}Sr/^{86}Sr$ values (Fig. 8a). A negative correlation between initial $^{87}Sr/^{86}Sr$ and ε_{Nd} values is present in the basalts but not in the picrites (Fig. 8a). The ε_{Nd} values of the LREE-enriched picrites from the Daying-Wumulaka region (this study) are significantly lower than that of a LREE-depleted picrite from the Jinping-Song Da region (Wang et al., 2007). Hanski et al. (2004) reported high ε_{Nd} values from 3.2 to 8 and near-chondritic γ_{Os} of $+0.02 \pm 0.40$ for LREE-depleted komatiites from the Song Da area in northern Vietnam, the southernmost part of the ELIP. These signatures, together with low initial $^{87}Sr/^{86}Sr$ ratios for the coeval LREE-depleted picrites from the same region (Wang et al., 2007), led Hanski et al. (2010) to conclude that the LREE-depleted ultramafic volcanic rocks in the ELIP originated from a depleted plume source and that crustal contamination was not important.

Compared to the coeval LREE-depleted picrites in the ELIP, the LREE-enriched picrites have lower ε_{Nd} values but similarly low initial $^{87}Sr/^{86}Sr$ ratios (Fig. 8a). These signatures, together with negative γ_{Os} values (-0.3 to -4.2, Zhang et al., 2008; Li et al., 2010) support the interpretations that crustal contamination was not important and that ancient sub-continental lithospheric mantle (SCLM) was involved in the genesis of the LREE-enriched picrirtes. Ancient SCLM is commonly characterized by the combination of LREE enrichments, mildly negative γ_{Os} values (average -11), intermediate ε_{Nd} values (mostly from 0 to 5) and low intitial $^{87}Sr/^{86}Sr$ ratios (Walker et al., 1989; Pearson et al., 1995; Shirey and Walker, 1998). The conclusion of insignificant crustal contamination in the Emeishan LREE-enriched picrites is also supported by the lack of correlations between initial $^{87}Sr/^{86}Sr$ ratios, and the primitive mantle-normalized Th/Yb and Nb/Th ratios (Fig. 8b and c). Crustal materials commonly have much higher Th/Yb and $^{87}Sr/^{86}Sr$ ratios, and much lower Nb/Th ratios than uncontaminated mantle-derived magmas. As a result, good correlations between these parameters are expected for a suite of rocks formed by magmas with variable degrees of crustal contamination, such as the coeval basalts (Fig. 8b and c).

In summary, both crustal contamination and source mantle heterogeneity played an important role in the differentiation of the Emeishan flood basalts. In contrast, the chemical variations in the coeval picrites mainly reflect source mantle heterogeneity. As shown in Fig. 8d, the primitive mantle-normalized $(Pt/Pd)_n$ ratios of the Emeishan picrites are highly variable from 0.2 to 1.1 but show no correlation with ε_{Nd} values. In addition, the $(Pt/Pd)_n$ ratio of a LREE-depleted picrite is within the range of the coeval LREE-enriched picrites (Fig. 8d). These features indicate that the different mantle components involved in the generation of the different types of picrites did not have systematically different $(Pt/Pd)_n$ ratios.

5.2. PGE fractionation during crystallization

As pointed out by Wang et al. (2007), whole-rock Cr content and Mg# [$MgO/(MgO + FeO^{total})$, molar] are

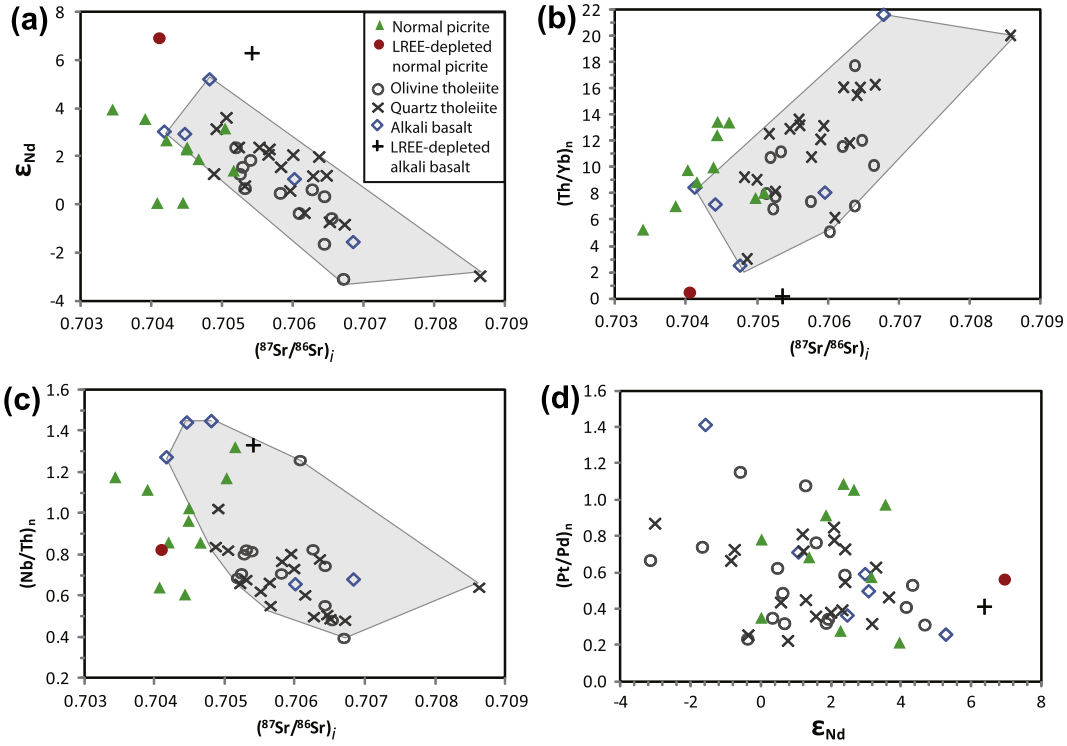

Fig. 8. Relationships between ε_{Nd}, initial $^{87}Sr/^{86}Sr$, and primitive mantle-normalized Th/Yb and Nb/Th for different types of basalts and picrites from the Emeishan large igneous province. Data are from this study and previous studies given in Table S3. The primitive mantle values are from Sun and McDonough (1989).

good fractionation indexes for the Emeishan flood basalts and picrites (Fig. 9a). Variations in Cr contents and Mg# in the picrites are due to variable amounts of Cr spinel inclusions, olivine phenocrysts and the transporting magma. In the coeval basalts such variations are related to variable amounts of magnetite inclusions, clinopyroxene phenocrysts and the transporting magmas, which are more evolved than those of the coeval picrites. No correlation between the primitive mantle-normalized $(Pt/Pd)_n$ ratios and whole-rock Mg# is present in the Emeishan basalts and picrites (Fig. 9b). In contrast, negative correlations exist between PPGE/IPGE and whole-rock Mg# or Cr contents (Fig. 9c–f). In the plots we used Ru instead of a more commonly chosen element, Ir, to represent IPGE. One of the reasons for our choice is the fact that decoupling between Ir and other IPGE exists at low concentrations in the Emeishan basalts (see Fig. 7d). Another uncertainty with Ir is that it may occur as Ir-dominant alloys in ultramafic magma (Barnes and Fiorentini, 2008). In contrast, Cr-spinel can accommodate a large proportion of Ru in ultramafic magma and hence it is more difficult to crystallize discrete Ru minerals in the magma (Locmelis et al., 2011). Osmium would also be a good choice but not all the analyses in the database have the results for this element. The negative correlations shown in Fig. 9c–f suggest that IPGE and PPGE are compatible and incompatible, respectively, during fractional crystallization of Cr-spinel, olivine, clinopyroxene and magnetite from magma. The experiments conducted at oxidation states relevant to the Emeishan magma plumbing systems (FMQ–2 to FMQ+4, Pang et al., 2008) indicate that Pt and Pd are incompatible in Cr-spinel, olivine and magnetite (solid–liquid partition coefficient, D, of <0.2 for all these phases) and that IPGE are compatible in both Cr-spinel and magnetite but only slightly compatible in olivine (D close to 2) (Capobianco and Drake, 1990; Capobianco et al., 1994; Brenan et al.,

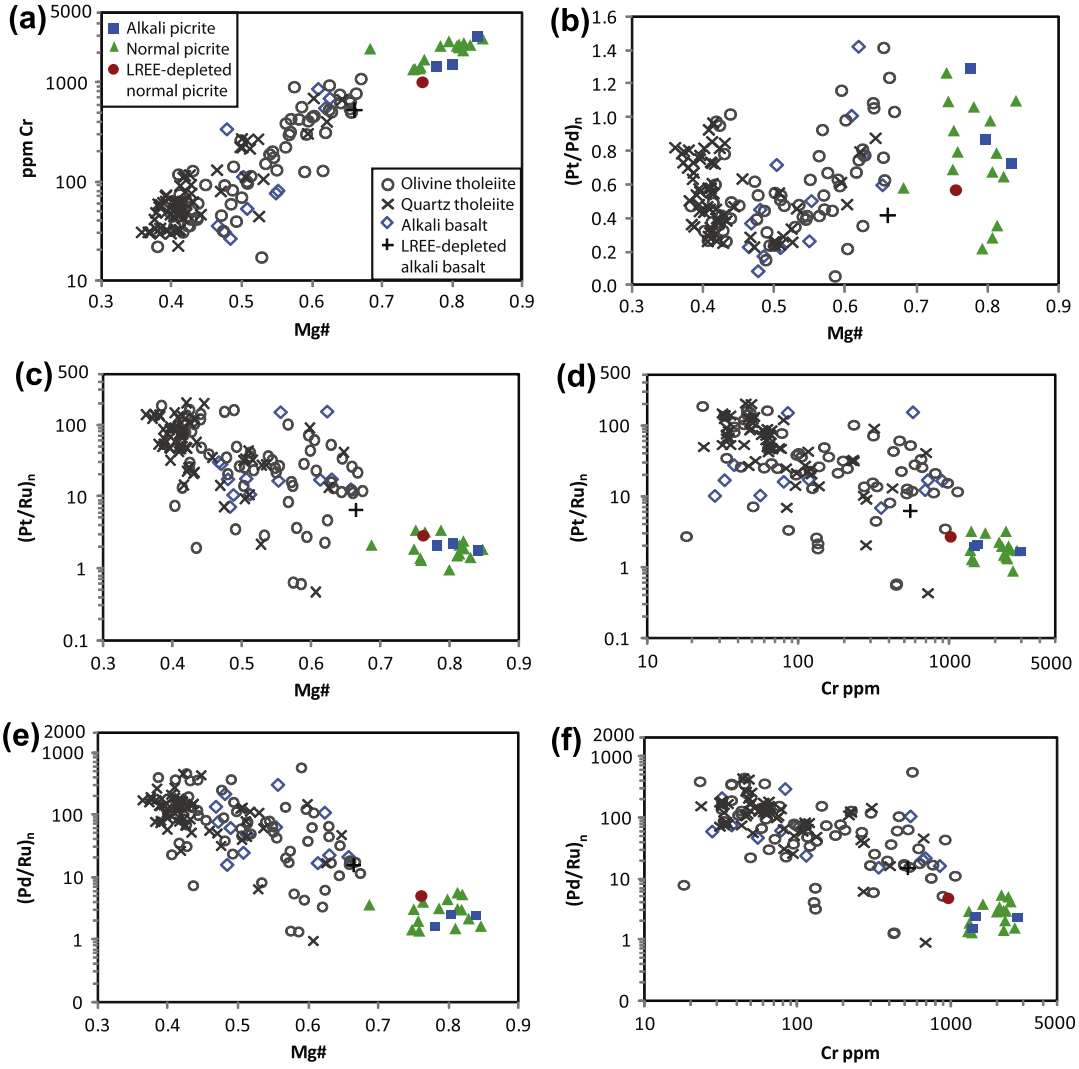

Fig. 9. Relationships between primitive mantle-normalized PGE ratios and fractionation indexes (Mg# and Cr content) for different types of basalts and picrites from the Emeishan large igneous province. Data are from this study and previous studies given in Table S3. The primitive mantle values are from Barnes and Maier (1999).

2003, 2005, 2012; Righter et al., 2004; Park et al., 2012). The $D^{\text{Spl-melt}}$ values of IPGE increase with oxygen fugacity and are hence positively correlated with $Fe^{3+}/(Fe^{3+} + Cr)$ in Cr-spinel (Brenan et al., 2012). The $Fe^{3+}/(Fe^{3+} + Cr)$ ratios of Cr-spinel inclusions in olivine phenocrysts from the picrites in the Daying area (see Fig. 1) vary between 0.15 and 0.3 (Li et al., 2008). The $D^{\text{Spl-melt}}$ values of IPGE for this type Cr-spinel are predicted to be 30–100 according to the experimental results of Brenan et al. (2012). The experimental $D^{\text{Spl-melt}}$ values of IPGE for magnetite under the conditions that are relevant to natural basaltic systems are >100 (Capobianco and Drake, 1990; Capobianco et al., 1994; Righter et al., 2004).

5.3. PGE depletion in magma

Depletion of Pd relative to Cu in mafic–ultramafic volcanic rocks is a good indicator of sulfide segregation from magma (Vogel and Keays, 1997) owning to much higher sulfide-magma partition coefficients for Pd than Cu ($D^{\text{Pd}} \sim 10^5$, $D^{\text{Cu}} \sim 10^3$, see a compilation by Naldrett (2011). As shown in Fig. 10a, some of the Emeishan basalts are significantly depleted in Pd relative to Cu and plot in the S-saturated field of Vogel and Keays (1997), being in this respect similar to MORB (Bézos et al., 2005) and the PGE-depleted lavas from the Siberian Traps (Lightfoot and Keays, 2005). In the ELIP, the basalts that are significantly depleted in Pd are characterized by 10^4Pd/Yb ratios less than 100 (Fig. 10b and c). In the Emeishan flood basalt province, Pd-depletion is observed more frequently in the less fractionated samples (i.e., higher Mg# and Cr contents) than the most fractionated samples (Fig. 10b and c), suggesting that fractional crystallization did not play a critical role in inducing sulfide saturation in the basaltic magmas.

Depletion of Ir relative to Ru in some of the Emeishan basalts (see Fig. 7d) may have resulted from segregation of Ir-dominant phases during magma evolution (cf, picrites and komatiites: Keays, 1995; Barnes and Fiorentini, 2008) or a much higher sulfide-magma D value for Ir than Ru. As shown in Fig. 10d, the primitive mantle-normalized $(Ir/Ru)_n$ values for the Pd-depleted samples, which are inferred to have experienced sulfide segregation (see Fig. 10a), are within the range of other samples. This suggests that sulfide segregation was not the primary cause of Ir–Ru decoupling in the Emeishan basalts.

As shown in Fig. 11a and b, in the ELIP the Pd-depleted basalts are among those with relatively high initial $^{87}Sr/^{86}Sr$ values and low $(Nb/Th)_n$ ratios. It is important to note that not all of the samples with elevated initial $^{87}Sr/^{86}Sr$ values and low $(Nb/Th)_n$ ratios are depleted in Pd. This implies that sulfide saturation was caused by crustal contamination but not all types of crustal contamination induced sulfide saturation. Based on the relationships between PGE depletion and different types of crustal contamination in the Siberian and Deccan Trap basalts, Keays and Lightfoot (2010) concluded that crustal sulfur is required to induce

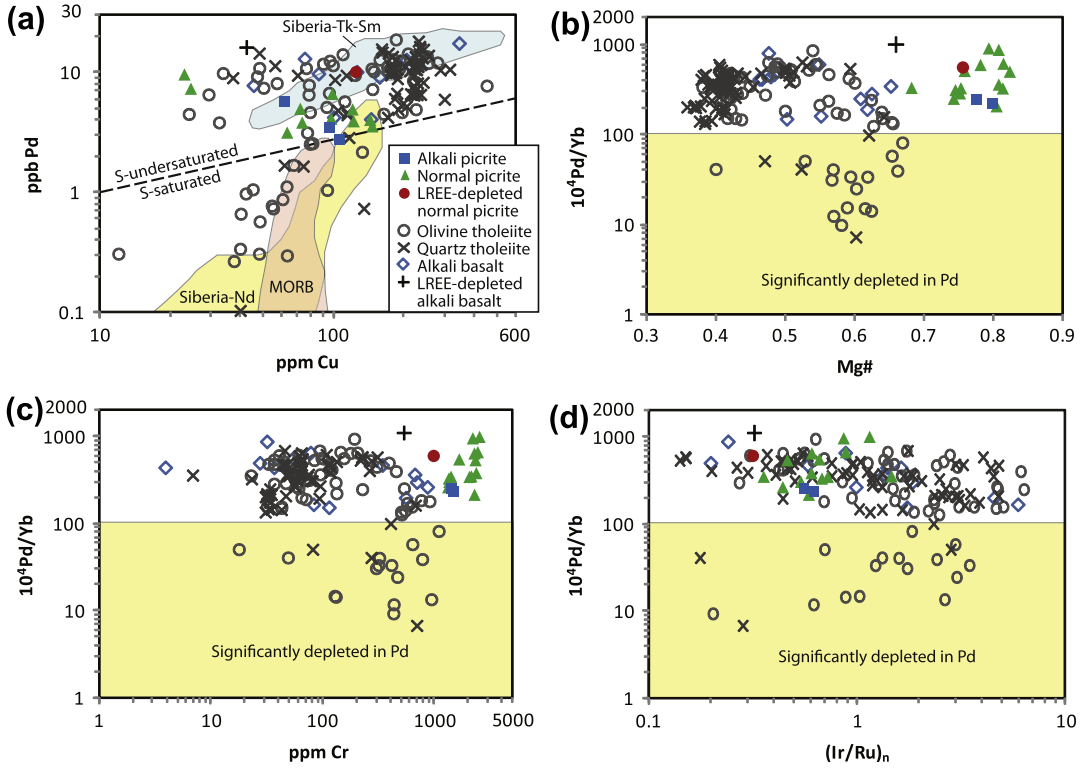

Fig. 10. Plots of Pd versus Cu (a), 10^4Pd/Yb versus Mg# (b), 10^4Pd/Yb versus Cr (c), and 10^4Pd/Yb versus primitive mantle-normalized Ir/Ru for different types of basalts and picrites from the Emeishan large igneous province. Data are from this study and previous studies given in Table S3. The primitive mantle values are from Barnes and Maier (1999). The division for S-saturated and S-undersaturated basalts is from Vogel and Keays (1997).

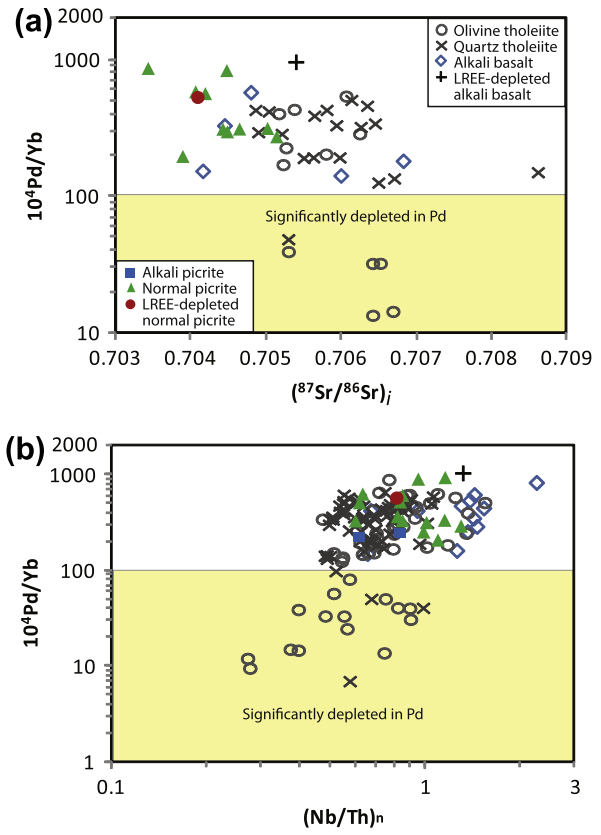

Fig. 11. Relationships between 10^4Pd/Yb, initial $^{87}Sr/^{86}Sr$ and primitive mantle-normalized Nb/Th for different types of basalts and picrites from the Emeishan large igneous province. Data are from this study and previous studies given in Table S3. The primitive mantle values are from Sun and McDonough (1989).

significant sulfide oversaturation. This conclusion is consistent with the results from the Emeishan flood basalts.

6. MODELING

6.1. Liquid composition and temperature

A picrite (Fig. 3a) is a mixture of olivine phenocrysts crystallized at depth and the transporting magma, which was quenched to form the groundmass upon eruption. Interaction between olivine phenocrysts and the transporting magma during magma ascent formed the Fo-poor rims of olivine phenocrysts (Fig. 3b and c). The composition of the transporting magma changed with time as this process progressed but its final composition (FeO/MgO ratio) upon eruption can be estimated from the outermost rims of olivine phenocrysts. The major element compositions of the transporting magma can be calculated if the following constraints are known: (1) the olivine–liquid Fe–Mg exchange coefficient [K_D, $(FeO/MgO)^{Ol}/(FeO/MgO)^{Liq} = 0.3$ according to Roeder and Emslie (1970)], (2) the average outermost rim composition of olivine phenocrysts, (3) the bulk composition of olivine phenocrysts, and (4) whole-rock composition. We have selected a relatively fresh picrite sample (DY8-8, Fig. 3a) that is free of clinopyroxene phenocrysts from the Daying area (see Fig. 1) to estimate the composition of the transporting magma. The total amount of olivine phenocrysts calculated based on the above constraints is 42 wt.%, which is in excellent agreement with the result from volume analysis (41 vol.%). The final composition of the transporting magma is listed in Table 4. It contains 8 wt.% MgO and 9.9 wt.% FeO, similar to the compositions of the least evolved basalts in the region (see Xu et al., 2001).

A primary magma is defined as a mantle-derived melt before undergoing fractional crystallization and crustal assimilation. The primary magma of the Daying picrite can be estimated by incrementally adding olivine with composition varying from Fo_{83} to $Fo_{92.5}$ to the transporting magma until the magma composition is in equilibrium with olivine phenocrysts having the maximum forsterite content, this being $Fo_{92.5}$. The total amount of olivine (weighted average Fo = 89 mol%) that is required to be added to the transporting magma is 33 wt.%, which is 9 wt.% less than the actual observed value in the sample. The MgO content of the estimated primary magma is 21 wt.% (Table 4), similar to the composition of most primitive melt inclusions in olivine phenocrysts from a picrite sample from the nearby area (Hanski et al., 2010). The mantle potential temperature (T_P; McKenzie and Bickle, 1988) of the primary magma is estimated to be 1590 °C using the equation of Herzberg and Gazel (2009). The estimated mantle potential temperature based on the primary magma is 240 °C higher than the average ambient mantle temperature (1350 °C, Herzberg et al., 2007), supporting the popular plume model for the ELIP. Notice that in our calculation we used a K_D, $(FeO/MgO)^{Ol}/(FeO/MgO)^{Liq}$ of 0.3 from Roeder and Emslie (1970). Some researchers (e.g., Kushiro and Mysen, 2002) suggested a higher K_D value up to 0.34 for high-Mg liquids. The MgO content in the modeled primary magma will increase proportionally if a higher K_D value is used in our calculation.

6.2. PGE abundances in primary magma

One way to estimate the abundance of PGE in the primary magma is to adjust for the effects of excess amounts of Cr-spinel and olivine phenocrysts in a picrite sample. The amount of excess olivine phenocrysts in a selected picrite sample (DY8-8) is estimated to be 9 wt.% (see above). It is more difficult to estimate the amount of excess Cr-spinel in the sample due to lack of required constraints. However, it is reasonable to use the lowest Cr concentration in the same type of picrites as a baseline. The lowest Cr content in the picrites from the Daying area is 1400 ppm (Table 1). In comparison, the Cr content in the selected sample (DY8-8) is 1000 ppm higher. This corresponds to an excess amount of 0.003 wt.% Cr-spinel in the sample based on the Cr-spinel composition of the sample given by Li et al. (2008). We have adjusted the effects from excess Cr-spinel and olivine phenocrysts in the sample using the partition coefficients that are consistent with the experimental results of Brenan et al. (2003, 2012) and empirical data from komatiites (Puchtel and Humayun, 2001; Puchtel et al., 2004; Barnes and Fiorentini, 2008), i.e., Cr-spinel/liquid:

Table 4
Compositions of magmas estimated from a primitive picrite sample from the Emeishan large igneous province (oxides in wt.%, PGE in ppb).

Sample	SiO_2	Cr_2O_3	TiO_2	Al_2O_3	NiO	FeO^T	MgO	MnO	CaO	Na_2O	K_2O	P_2O_5	Total
Picrite (DY8-8)	44.50	0.37	0.79	9.07	0.15	10.86	24.54	0.15	8.25	0.96	0.19	0.18	100.00
Bulk olivine separates (by XRF)	40.65	0.13	0.02	0.15	0.26	10.40	47.06	0.12	0.35	0.08	0.01	0.02	99.24
Magma	SiO_2	Cr_2O_3	TiO_2	Al_2O_3	Fe_2O_3	FeO	MgO	MnO	CaO	Na_2O	K_2O	P_2O_5	Total
Transporting magma[a]	46.96	0.54	1.34	15.47	1.41	9.89	8.01	0.17	13.93	1.65	0.33	0.31	100.00
Primary magma[b]	44.86	0.39	0.90	10.47	0.95	10.14	21.04	0.15	9.53	1.11	0.22	0.21	100.00
	Ir	Ru	Rh	Pt	Pd								
Primary magma[c]	1.32	1.96	0.65	5.79	7.93								

[a] The composition of transporting magma was estimated by subtracting the composition olivine phenocrysts (olivine separate) from whole rock composition until it is in equilibrium with the rim (average Fo = 83 mol%) of olivine phenocrysts, i.e., olivine–iquid Mg–Fe exchange coefficient $K_D = 0.3$ (Roeder and Emslie, 1970). Fe_2O_3/FeO in magma is adjusted for FMQ buffer and liquid temperature at 1 bar estimated using the MELTS program of Ghiorso and Sack (1995).

[b] The composition of primary magma was calculated by incrementally adding olivine with composition varying from Fo_{83} to $Fo_{92.5}$ to the transporting magma until the composition is in equilibrium with the most primitive olivine in the sample (i.e., $Fo_{92.5}$).

[c] Estimated from whole-rock compositions by adjusting the effects of excessive Cr-spinel and olivine phenocrysts in the sample.

$D^{Ir} = 15$, $D^{Ru} = 30$, $D^{Rh} = 60$, $D^{Pt,Pd} = 0.1$; olivine/liquid: $D^{Ir,Ru,Rh} = 0.5$, $D^{Pt,Pd} = 0.05$. The estimated PGE abundances in the primary magma are listed in Table 4.

6.3. PGE fractionation during mantle melting

The primitive mantle-normalized PGE patterns for the primary magma and the related whole-rock sample are similar (Fig. 12). They all show significant depletions in Ir and Ru relative to Pd. Depletions of Ir, Ru and Rh relative to Pt and Pd in some primitive volcanic rocks such as picrites and komatiites, which are widely known, have been commonly attributed to the occurrence of potential Ir–Ru–Rh alloys in the mantle during high-degree mantle melting (e.g., Keays, 1995). More recently, however, some researchers (e.g., Bockrath et al., 2004) have suggested that monosulfide solid solution (MSS), rather than Ir–Ru–Rh alloys, is responsible for PGE fractionation during mantle melting because (1) MSS is stable under the upper mantle conditions and (2) Ir, Ru and Rh are compatible whereas Pt and Pd are incompatible in MSS. A limitation with this new hypothesis is that no sulfides, including MSS, can be present in the mantle during high degrees of mantle partial melting that are required to generate picritic and komatiitic magmas. Recent calculations by Naldrett (2011), who used the mantle composition of Hart and Zindler (1986), an average S content of 200 ppm in the mantle (Palme and O'Neill, 2003), the pMELTS program of Ghiorso et al. (2002) and the SCSS (sulfur content at sulfur saturation) equation of Li and Ripley (2009) indicate that about 17% partial melting is required to consume all sulfides in the mantle and that the mantle melt contains slightly less than 21 wt.% MgO. Thus, depletions of IPGE relative to Pt and Pd in the Emeishan picrites and the primary magma are more likely due to the presence of residual Ir-Ru alloys instead of MSS in the mantle.

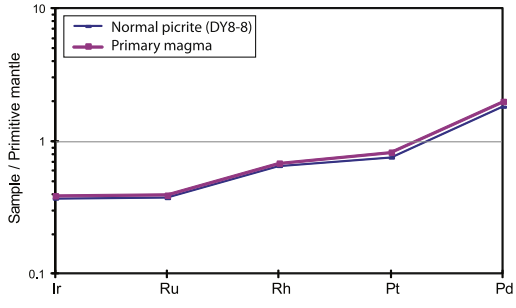

Fig. 12. Primitive mantle-normalized PGE patterns for a primitive picrite and the primary magma estimated based on the composition of this sample. The primitive mantle values are from Barnes and Maier (1999).

7. CONCLUSIONS

Important conclusions from this study are summarized below:

(1) The $^{40}Ar/^{39}Ar$ ages of 155–204 Ma for a picrite sample from the Daying area eliminate the possibility that the Daying picrites are Cenozoic picritic porphyries. Like the coeval Permian basalts, variably younger $^{40}Ar/^{39}Ar$ ages than their eruption ages are due to multiple events of post-eruption hydrothermal alteration.

(2) The primary magma of the Daying picrites contains 21 wt.% MgO and has a mantle potential temperature 240 °C higher than the average ambient mantle temperature, supporting a plume origin.

(3) The degree of mantle melting required to generate such ultramafic magma is >17%. At such high degree of partial melting no sulfides are expected to be left behind in the mantle. Thus, depletions of IPGE relative to Pt and Pd in the picrites and the primary magma are most likely due to residual IPGE alloys instead of MSS in the mantle.

(4) Similarly low initial $^{87}Sr/^{86}Sr$ ratios (<0.7057) but variable ε_{Nd} values (0–7) for different types of picrites (LREE depleted and enriched) in the ELIP suggest that crustal contamination is negligible but source

mantle variation is responsible for their chemical diversity. A depleted plume source and an ancient SCLM are inferred to be the most important end-members involved in the genesis of the Emeishan picrites.

(5) No picrites in the ELIP that have been analyzed to date are depleted in both Pt and Pd, suggesting that they formed by S-undersaturated magmas. The Pt/Pd ratios in the samples are highly variable but do not show any correlation with rock type variation, suggesting that Pt/Pd ratios are not dramatically different between the different mantle components involved.

(6) The coeval basalts are variably contaminated with crustal materials and more fractionated than the transporting magma of picrites, which makes them less useful than the coeval picrites in studying source mantle heterogeneity.

(7) The data from the Emeishan basalts and picrites confirm that Os, Ir and Ru are compatible, and Pd, Pt and Rh are incompatible during Cr-spinel and olivine crystallization from intra-plate mafic–ultramafic magmas.

(8) Significant Pt + Pd depletions are present in some of the basalts with clear crustal contamination signatures, but not all the basalts with such signatures are significantly depleted in Pt + Pd, suggesting that only certain types of contamination, perhaps only those involving crustal sulfur, were able to induce significant sulfide oversaturation in the magma.

(9) The PGE-depleted basalts in the ELIP are not restricted to the most fractionated samples. In fact, the majority of the most fractionated basalts are not significantly depleted in Pt + Pd. These features suggest that fractional crystallization alone is not enough to induce significant sulfide oversaturation in the magma.

(10) Significant depletion of Ir relative to Ru is present in some of the basalts regardless of sulfide saturation in the parental magmas. This is consistent with segregation of Ir-dominant alloys from the magmas prior to eruption.

ACKNOWLEDGMENTS

This work was financially supported by the Knowledge-innovation Program of the Chinese Academy of Sciences (KZCX2-YW-Q04-06), the National 973 Program of China (2012CB416804), the National Science Foundation of China (Grants 40973039, 40730420), the "Hundred Talents" Project of the Chinese Academy of Sciences to Qi (KZCX2-YW-BR-09) and a research Grant from the State Key Laboratory of Ore Deposit Geochemistry of China (200905). Constructive reviews from Steve Barnes and Eero Hanski are greatly appreciated.

APPENDIX A. SUPPLEMENTARY DATA

Supplementary data associated with this article can be found, in the online version, at http://dx.doi.org/10.1016/j.gca.2012.04.046.

REFERENCES

Ali J. R., Lo C. H., Thompson G. M. and Song X.-Y. (2004) Emeishan basalt Ar–Ar overprint ages define several tectonic events that affected the western Yangtze platform in the Mesozoic and Cenozoic. *J. Asian Earth Sci.* **23**, 163–178.

Ali J. R., Fitton J. G. and Herzberg C. (2010) Emeishan large igneous province (SW China) and the mantle-plume up-doming hypothesis. *J. Geol. Soc. London* **167**, 953–959.

Anh T. V., Pang K.-N., Chung S.-L., Lin H.-M., Hoa T. T., Anh T. T. and Yang H.-J. (2011) The Song Da magmatic suite revisited: a petrologic, geochemical and Sr–Nd isotopic study on picrites, flood basalts and silicic volcanic rocks. *J. Asian Earth Sci.* **42**, 1341–1355.

Barnes S. J. and Fiorentini M. L. (2008) Iridium, ruthenium and rhodium in komatiites: evidence for iridium alloy saturation. *Chem. Geol.* **257**, 44–58.

Barnes S.-J. and Maier W. D. (1999) The fractionation of Ni, Cu, and the noble metals in silicate and sulfide liquids. *Geological Association of Canada Short Course Notes* **13**, 69–106.

Bockrath C., Ballhaus C. and Holzheid A. (2004) Fractionation of the platinum-group elements during mantle melting. *Science* **305**, 1951–1953.

Brenan J. M., McDonough W. F. and Dalpe C. (2003) Experimental constraints on the partitioning of rhenium and some platinum-group elements between olivine and silicate melt. *Earth Planet. Sci. Lett.* **212**, 135–150.

Brenan J. M., McDonough W. F. and Ash R. (2005) An experimental study of the solubility and partitioning of iridium and osmium between olivine and silicate melt. *Earth Planet. Sci. Lett.* **237**, 855–872.

Brenan J. M., Finnigan C. F., McDonough W. F. and Homolova V. (2012) Experimental constraints on the partitioning of Ru, Rh, Ir, Pt and Pd between chromite and silicate melt: the importance of ferric iron. *Chem. Geol.* **302–303**, 16–32.

Bézos A., Lorand J.-P., Humler E. and Gros M. (2005) Platinum-group element systematics in mid-oceanic ridge basaltic glasses from the Pacific, Atlantic, and Indian Oceans. *Geochim. Cosmochim. Acta* **69**, 2613–2627.

Capobianco C. H. and Drake M. (1990) Partitioning of ruthenium, rhodium, and palladium between spinel and silicate melt and implications for platinum-group element fractionation trends. *Geochim. Cosmochim. Acta* **54**, 869–874.

Capobianco C. H., Hervig R. L. and Drake M. (1994) Experiments on crystal/liquid partitioning of Ru, Rh and Pd for magnetite and hematite solid solutions crystallized from silicate melt. *Chem. Geol.* **113**, 23–43.

Chung S.-L. and Jahn B. M. (1995) Plume–lithosphere interaction ingeneration of the Emeishan flood basalts at the Permian–Triassicboundary. *Geology* **23**, 889–892.

Chung S.-L., Lee T.-Y., Lo C.-H., Wang P.-L., Chen C.-Y., Yem N. T., Hoa T. T. and Wu G. (1997) Intraplate extension prior to continental extrusion along the Ailao Shan-Red River shear zone. *Geology* **25**, 311–314.

Chu Z., Chen F., Yang Y. and Guo J. (2009) Precise determination of Sm, Nd concentrations and Nd isotopic compositions at the nanogram level in geological samples by thermal ionization mass spectrometry. *J. Anal. Atom. Spectrom.* **24**, 1534–1544.

Ghiorso M. S. and Sack R. O. (1995) Chemical mass transfer in magmatic processes IV. A revised and internally consistent thermodynamic model for the interpolation and extrapolation of liquid–solid equilibria in magmatic systems at elevated temperatures and pressures. *Contrib. Mineral. Petrol.* **119**, 197–212.

Ghiorso M. S., Hirschmann M. M., Reiners P. W. and Kress V. C. (2002) The pMELTS: an revision of MELTS aimed at

improving calculation of phase relations and major element partitioning involved in partial melting of the mantle at pressures up to 3 GPa. *Geochem. Geophys. Geosys.* **3**, 1030.

Hanski E., Walker R. J., Huhma H., Polyakov G. V., Balykin P. A., Trong H. T. and Thi P. N. (2004) Origin of the Permo–Triassic komatiites, northwestern Vietnam. *Contrib. Mineral. Petrol.* **147**, 453–469.

Hanski E., Kamenetsky V. S., Luo Z.-Y., Xu Y.-G. and Kuzmin D. V. (2010) Primitive magmas in the Emeishan Large Igneous Province, southwestern China and northern Vietnam. *Lithos* **119**, 75–90.

Hart S. R. and Zindler A. (1986) In search of a bulk-Earth composition. *Chem. Geol.* **57**, 247–267.

Herzberg C. and Gazel E. (2009) Petrological evidence for secular cooling in mantle plumes. *Nature* **458**, 619–622.

Herzberg C., Asimow P. D., Arndt N., Niu Y. L., Lesher C. M., Fitton J. G., Cheadle M. J. and Saunders A. D. (2007) Temperatures in ambient mantle and plumes: Constraints from basalts, picrites, and komatiites. *Geochem. Geophys. Geosys.* **8**, Q02006. http://dx.doi.org/10.1029/2006GC001390.

Hou T., Zhang Z., Kusky T., Du Y., Liu J. and Zhao Z. (2011) A reappraisal of the high-Ti and low-Ti classification of basalts and petrogenetic linkage between basalts and mafic–ultramafic intrusions in the Emeishan Large Igneous Province, SW China. *Ore Geol. Rev.* **41**, 133–143.

Keays R. R. (1995) The role of komatiitic and picritic magmatism and S-saturation in the formation of ore deposits. *Lithos* **34**, 1–18.

Keays R. R. and Lightfoot P. C. (2010) Crustal sulfur is required to form magmatic Ni–Cu sulfide deposits: evidence from chalcophile element signatures of Siberian and Deccan Trap basalts. *Miner. Deposita* **45**, 241–257.

Kushiro I. and Mysen B. O. (2002) A possible effect of melt structure on the Mg–Fe^{2+} partitioning between olivine and melt. *Geochim. Cosmochim. Acta* **66**, 2267–2272.

Li C. and Ripley E. M. (2009) Sulfur contents at sulfide-liquid or anhydrite saturation in silicate melts: empirical equations and example applications. *Econ. Geol.* **104**, 405–412.

Li C., Ripley E. M., Tao Y. and Mathez E. A. (2008) Cr–spinel/melt and Cr–spinel/olivine nickel partition coefficients from basalts, picrites and intrusive rocks. *Geochim. Cosmochim. Acta* **72**, 1678–1684.

Li C., Thakurta J. and Ripley E. M. (2012) Low-Ca content and kink-banded texture are not unique for mantle olivine: evidence from the Duke Island Complex, Alaska. *Mineral. Petrol.* **104**, 147–153.

Li J., Xu J.-F., Suzuki K., He B., Xu Y.-G. and Ren Z.-Y. (2010) Os, Nd and Sr isotope and trace element geochemistry of the Muli picrites: insights into the mantle source of the Emeishan Large Igneous Province. *Lithos* **119**, 108–122.

Liang Q., Jing H. and Gregoire D. C. (2000) Determination of trace elements in granites by inductively coupled plasma mass spectrometry. *Talanta* **51**, 507–513.

Lo C., Chung S., Lee T. and Wu G. (2002) Age of the Emeishan flood magmatism and relations to Permian–Triassic boundary events. *Earth Planet. Sci. Lett.* **198**, 449–458.

Lightfoot P. C. and Keays R. R. (2005) Siderophile and chalcophile metal variations in flood basalts from the Siberian Trap, Noril'sk Region: implications for the origin of the Ni–Cu–PGE sulfide ores. *Econ. Geol.* **100**, 439–462.

Locmelis M., Pearson N. J., Barnes S. J. and Fiorentini M. L. (2011) Ruthenium in komatiitic chromite. *Geochim. Cosmochim. Acta* **75**, 3645–3661.

McKenzie D. and Bickle M. J. (1988) The volume and composition of melt generated by extension of the lithosphere. *J. Petrol.* **29**, 625–679.

Naldrett A. J. (2011) Fundamentals of magmatic sulfide deposits. *Rev. Econ. Geol.* **17**, 1–50.

Palme H. and O'Neill H. St. C. (2003) Cosmochemical estimates of mantle composition. In *Treatise on Geochemistry, Volume 2* (ed. R. W. Carlson, executive eds. H. D. Holland and K. K. Turekian, pp. 568). Elsevier, p. 1–38. ISBN 0-08-043751-6.

Pang K.-N., Li C., Zhou M.-F. and Ripley E. M. (2008) Abundant Fe–Ti oxide inclusions in olivine from the Panzhihua and Hongge layered intrusions, SW China: evidence for early saturation of Fe–Ti oxides in ferrobasaltic magma. *Contrib. Mineral. Petrol.* **156**, 307–321.

Pang K. N., Li C., Zhou M.-F. and Ripley E. M. (2009) Mineral compositional constraints on petrogenesis and oxide ore genesis of the late Permian Panzhihua layered gabbroic intrusion, SW China. *Lithos* **110**, 199–214.

Park J.-W., Campbell I. H. and Eggins S. M. (2012) Enrichment of Rh, Ru, Ir and Os in Cr spinels from oxidized magmas: Evidence from the Ambae volcano, Vanuatu. *Geochim. Cosmochim. Acta* **78**, 28–50.

Pearson D. G., Carlson R. W., Shirey S. B., Boyd F. R. and Nixon P. H. (1995) Stabilisation of Archaean lithospheric mantle: a Re–Os isotope study of peridotite xenoliths from the Kaapvaal craton. *Earth Planet. Sci. Lett.* **134**, 341–357.

Puchtel I. S. and Humayun M. (2001) Platinum group element fractionation in a komatiitic basalt lava lake. *Geochim. Cosmochim. Acta* **65**, 2979–2993.

Puchtel I. S., Humayun M., Campbell A. J., Sproule R. A. and Lesher C. M. (2004) Platinum group element geochemistry of komatiites from the Alexo and Pyke Hill areas, Ontario, Canada. *Geochim. Cosmochim. Acta* **68**, 1361–1383.

Righter K., Campbell A. J., Humayun M. and Hervig R. L. (2004) Partitioning of Ru, Rh, Pd, Re, Ir, and Au between Cr-bearing spinel, olivine, pyroxene and silicate melts. *Geochim. Cosmochim. Acta* **68**, 867–880.

Roeder P. L. and Emslie R. F. (1970) Olivine–liquid equilibrium. *Contrib. Mineral. Petrol.* **71**, 257–269.

Qi L. and Zhou M.-F. (2008) Platinum-group elemental and Sr–Nd–Os isotopic geochemistry of Permian Emeishan flood basalts in Guizhou Province, SW China. *Chem. Geol.* **248**, 83–103.

Qi L., Zhou M.-F. and Wang C. Y. (2004) Determination of low concentrations of platinum group elements in geological samples by ID-ICP-MS. *J. Anal. Atom. Spectrom.* **19**, 1335–1339.

Qi L., Zhou M.-F., Wang C. Y. and Sun M. (2007) Evaluation of the determination of Re and PGEs abundance of geological samples by ICP-MS coupled with a modified Carius tube digestion at different temperatures. *Geochem. J.* **41**, 407–414.

Qi L., Wang C. Y. and Zhou M.-F. (2008) Controls on the PGE distribution of Permian Emeishan alkaline and peralkaline volcanic rocks in Longzhoushan, Sichuan Province, SW China. *Lithos* **106**, 222–236.

Qiu H.-N. and Wijbrans J. R. (2008) The Paleozoic metamorphic history of the Central Orogenic Belt of China from $^{40}Ar/^{39}Ar$ geochronology of eclogite garnet fluid inclusions. *Earth Planet. Sci. Lett.* **268**, 501–514.

Roeder P. L. and Emslie R. F. (1970) Olivine–liquid equilibrium. *Contrib. Mineral. Petrol.* **29**, 275–289.

Shirey S. B. and Walker R. J. (1998) The Re–Os isotope system in cosmochemistry and high temperature geochemistry. *Ann. Rev. Earth Planet. Sci.* **26**, 423–500.

Simkin T. and Smith J. V. (1970) Minor-element distribution in olivine. *Jour. Geol.* **78**, 304–325.

Song X.-Y., Zhou M.-F., Hou Z., Cao Z., Wang W. and Li Y. (2001) Geochemical constraints on the mantle source of the upper Permian Emeishan continental flood basalts, southern China. *Int. Geol. Rev.* **43**, 213–225.

Song X.-Y., Zhou M.-F., Keays R. R., Cao Z.-M., Sun M. and Qi L. (2006) Geochemistry of the Emeishan flood basalts at Yangliuping, Sichuan, SW China: implications for sulfide segregation. *Contrib. Mineral. Petrol.* **152**, 53–74.

Song X.-Y., Qi H.-W., Robinson P. T., Zhou M.-F., Cao Z.-M. and Chen L.-M. (2008) Melting of the subcontinental lithospheric mantle by the Emeishan mantle plume; evidence from the basal alkaline basalts in Dongchuan, Yunnan, Southwestern China. *Lithos* **100**, 93–111.

Song X.-Y., Keays R. R., Xiao L., Qi H.-W. and Ihlenfeld C. (2009) Platinum-group element geochemistry of the continental flood basalts in the central Emeisihan Large Igneous Province, SW China. *Chem. Geol.* **262**, 246–261.

Sun S. S. and McDonough W. F. (1989) Chemical and isotopic systematics in ocean basalt: implication for mantle composition and processes. *Geol. Soc. Spec. Pub.* **42**, 313–345.

Tao Y., Li C., Hu R., Ripley E. M., Du A. and Zhong H. (2007) Petrogenesis of the Pt–Pd mineralized Jinbaoshan ultramafic intrusion in the Permian Emeishan Large Igneous Province, SW China. *Contrib. Mineral. Petrol.* **153**, 321–337.

Tao Y., Li C., Song X.-Y. and Ripley E. M. (2008) Mineralogical, petrological and geochemical studies of the Limahe mafic–ultramatic intrusion and the associated Ni–Cu sulfide ores, SW China. *Miner. Deposita* **43**, 849–872.

Tao Y., Li C., Hu R., Qi L., Qu W. and Du A. (2010) Re–Os isotopic constraints on the genesis of the Limahe Ni–Cu deposit in the Emeishan large igneous province, SW China. *Lithos* **119**, 137–146.

TGT-YBGR (Third Geological Team, Yunnan Bureaus of Geology and Resources) (1993) 1:50000 Geological map of Dayingjie.

Vogel D. C. and Keays R. R. (1997) The application of platinum group geochemisty in constraining the source of basalt magmas: results from the Newer Volcanic Province, Victoria, Australia. *Chem. Geol.* **136**, 181–204.

Walker R. J., Carlson R. W., Shirey S. B. and Boyd F. R. (1989) Os, Sr, Nd, and Pb isotope systematics of southern African peridotite xenoliths: implications for the chemical evolution of subcontinental mantle. *Geochim. Cosmochim. Acta* **53**, 1583–1595.

Wang C. Y., Zhou M.-F. and Qi L. (2007) Permian basalts and mafic intrusions in the Jinping (SW China)–Song Da (northern Vietnam) district: mantle sources, crustal contamination and sulfide segregation. *Chem. Geol.* **243**, 317–343.

Wang C. Y., Zhou M.-F. and Qi L. (2011) Chalcophile element geochemistry and petrogenesis of high-Ti and low-Ti magmas in the Permian Emeishan large igneous province, SW China. *Contrib. Mineral. Petrol.* **161**, 237–254.

Wijbrans J. R., Pringle M. S., Koppers A. A. P. and Scheveers R. (1995) Argon geochronology of small samples using the Vulkaan argon laserprobe. *Proc. K. Ned. Akad. Wet. Ser. C Biol. Med. Sci.* **98**, 185–218.

Xiao L., Xu Y. G., Mei H. J., Zheng Y. F., He B. and Pirajno F. (2004) Distinct mantle sources of low-Ti and high-Ti basalts from the Eastern Emeishan Large Igneous Province, SW China: implications for plume–lithosphere interaction. *Earth Planet. Sci. Lett.* **228**, 525–546.

Xu Y., Chung S., Jahn B. and Wu G. (2001) Petrologic and geochemical constraints on the petrogenesis of Permian–Triassic Emeishan flood basalts in southern China. *Lithos* **58**, 145–168.

Yoder J. R. H. S. and Tilley C. E. (1962) Origin of basalt magmas: an experimental study of natural and synthetic systems. *J. Petrol.* **3**, 342–532.

Zhang H. F., Sun M., Lu F. X., Zhou X. H., Zhou M.-F., Liu Y. S. and Zhang G. H. (2001) Moderately depleted lithospheric mantle underneath the Yangtze Block: evidence from a garnet lherzolite xenolith in the Dahongshan kimberlite. *Geochem. J.* **35**, 315–331.

Zhang Z. C., Mao J. W., Mahoney J. J., Wang F. and Qu W. (2005) Platinum group elements in the Emeishan large igneous province, SW China: implications for mantle sources. *Geochem. J.* **39**, 371–382.

Zhang Z. C., Mahoney J. J., Mao J. W. and Wang F. S. (2006) Geochemistry of picritic and associated flows of the western Emeishan flood basalt province, China. *J. Petrol.* **47**, 1997–2019.

Zhang Z. C., Zhi X., Chen L., Saunders A. D. and Reichow M. K. (2008) Re–Os isotopic compositions of picrites from the Emeishan flood basalt province, China. *Earth Planet. Sci. Lett.* **276**, 30–39.

Zhong H., Campbell I. H., Zhu W.-G., Allen C. M., Hu R.-Z., Xie L.-W. and He D. F. (2011a) Timing and source constraints on the relationship between mafic and felsic intrusions in the Emeishan large igneous province. *Geochim. Cosmochim. Acta* **75**, 1374–1395.

Zhong H., Qi L., Hu R.-Z., Zhou M.-F., Gu T. Z., Zhu W.-G., Liu B.-G. and Chu Z. (2011b) Rhenium-osmium isotope and platinum-group elements in the Xinjie layered intrusion, SW China: implications for source mantle composition, mantle evolution, PGE fractionation and mineralization. *Geochim. Cosmochim. Acta* **75**, 1621–1640.

Zhou M.-F., Malpas J., Song X. Y., Robinson P. T., Sun M., Kennedy A. K., Lesher C. M. and Keays R. R. (2002) A temporal link between the Emeishan large igneous province (SW China) and the end-Guadalupian mass extinction. *Earth Planet. Sci. Lett.* **196**, 113–122.

Zhou M.-F., Arndt N. T., Malpas J., Wang C. Y. and Kennedy A. K. (2008) Two magma series and associated ore deposit types in the Permian Emeishan large igneous province, SW China. *Lithos* **103**, 352–368.

Associate editor: Anders Meibom